Biomaterials 31 (2010) 4094–4103

Contents lists available at ScienceDirect

Biomaterials

journal homepage: www.elsevier.com/locate/biomaterials

Quantum dots labeling using octa-arginine peptides for imaging of adipose tissue-derived stem cells

Hiroshi Yukawa [a,*], Yukimasa Kagami [b], Masaki Watanabe [b], Koichi Oishi [a], Yoshitaka Miyamoto [a], Yukihiro Okamoto [b,c], Manabu Tokeshi [b,c], Noritada Kaji [b], Hirofumi Noguchi [d], Kenji Ono [e], Makoto Sawada [e], Yoshinobu Baba [b,c,f,g,h], Nobuyuki Hamajima [i], Shuji Hayashi [a]

[a] Department of Advanced Medicine in Biotechnology and Robotics, Nagoya University Graduate School of Medicine, Nagoya University, Higashi-ku, Nagoya 461-0047, Japan
[b] Department of Applied Chemistry, Nagoya University Graduate School of Engineering, Nagoya University, Furo-cho, Chikusa-ku, Nagoya 464-8603, Japan
[c] MEXT Innovative Research Center for Preventive Medical Engineering, Nagoya University, Furo-cho, Chikusa-ku, Nagoya 464-8603, Japan
[d] Baylor Institute for Immunology Research, Baylor Research Institute, 3434 Live Oak St., Dallas, TX 75204, USA
[e] Research Institute of Environmental Medicine, Stress Adaption and Protection, Nagoya University, Furo-cho, Chikusa-ku, Nagoya, 464-8601, Japan
[f] Plasma Nanotechnology Research Center, Nagoya University, Furo-cho, Chikusa-ku, Nagoya 464-8603, Japan
[g] Health Technology Research Center, National Institute of Advanced Industrial Science and Technology (AIST), Hayashi-cho 2217-14, Takamatsu 761-0395, Japan
[h] Institute for Molecular Science, National Institutes of Natural Sciences, Myodaiji Nishigo-naka 38, Okazaki 444-8585, Japan
[i] Department of Preventive Medicine, Biostatistics and Medical Decision Making, Nagoya University Graduate School of Medicine, Nagoya 466-8550, Japan

ARTICLE INFO

Article history:
Received 30 October 2009
Accepted 27 January 2010
Available online 19 February 2010

Keywords:
Semiconductor
Quantum dots (QDs)
Cell-penetrating peptides (CPPs)
In vivo imaging
Adipose tissue-derived stem cells (ASCs)

ABSTRACT

Quantum dots (QDs) have been used to study the effects of fluorescent probes for biomolecules and cell imaging. Adipose tissue-derived stem cells, which carry a relatively lower donor site morbidity, while yielding a large number of stem cells at harvest, were transduced with QDs using the octa-arginine peptide (R8) cell-penetrating peptide (CPP). The concentration ratio of QDs:R8 of 1×10^4 was optimal for delivery into ASCs. No cytotoxicity was observed in ASCs transduced with less than 16 nM of QDs655. In addition, >80% of the cells could be labeled within 1 h and the fluorescent intensity was maintained at least for 2 weeks. The ASCs transduced with QDs using R8 could be differentiated into both adipogenic and osteogenic cells, thus suggesting that the cells maintained their stem cell potency. The ASCs labeled with QDs using R8 were further transplanted subcutaneously into the backs of mice or into mice through the tail vein. The labeled ASCs could be imaged with good contrast using the Maestro *in vivo* imaging system. These data suggested that QD labeling using R8 could be utilized for the imaging of ASCs.

1. Introduction

Quantum dots (QDs) are inorganic probes that consist of CdSe/ZnS-core/shell semiconductor nanocrystals. QDs have several distinctive advantages in comparison to conventional organic labels such as a high luminance, resistance to photobleaching (long time labeling), a range of excitation wavelengths and narrower emission bandwidths [1–4]. According to these characteristics, QDs have recently been investigated as fluorescent probes for biomolecules and live cells, and are expected to be used in medical applications for diagnostics [5,6]. Various approaches have been applied to label cells with QDs, such as microinjection, electroporation, liposome-based transduction and special peptide delivery [7–11].

The transduction of QDs into cells using cell-penetrating peptides (CPPs) has been established and is thought to a useful technique because of the low cytotoxicity and high transduction efficiency. Yun Lei et al. showed that Tat peptide conjugated QDs could be transduced into mesenchymal stem cells [12]. Jui-Chih Chang et al. showed that Pep-1 labeled QDs could be transduced into stem cells and remained for about one month [13]. However, few detailed studies have so far explored the appropriate ratio of QDs and peptide, uptake time, cell function *in vitro* and application of *in vivo* imaging.

Regenerative medicine is expected to overcome the shortage of donated organs, donor site morbidity and immune reaction [14]. Many kinds of stem cells have been discovered already and provided numerous applications in regenerative medicine. Mesenchymal stem cells (MSCs) and progenitor cells are detected in various tissues, including umbilical cord blood, bone marrow, periodontal ligament and adipose tissue.

Bone marrow-derived stem cells (BMSCs) have the ability to differentiate into multiple mesenchymal cells such as cardiomyocytes, chondrocytes, osteoblasts and adipocytes.

* Corresponding author. Tel.: +81 52 719 1975; fax: +81 52 719 1977.
E-mail address: hiroshiy@med.nagoya-u.ac.jp (H. Yukawa).

0142-9612/$ - see front matter © 2010 Elsevier Ltd. All rights reserved.
doi:10.1016/j.biomaterials.2010.01.134

Therefore, BMSCs have been considered to be an important source of stem cells for use in regenerative medicine.

Recently, adipose tissue-derived stem cells (ASCs) have been increasingly recognized as multipotent stem cells and as an alternative source of BMSCs [15]. ASCs are easier to obtain in abundance by minimally invasive harvest procedures such as lipoaspiration with local anesthesia. In addition, ASCs possess the ability of self-renewing and differentiating into various mesenchymal cell types, while also secreting significant levels of many potent growth factors and cytokines, such as vascular endothelial growth factor (VEGF) and hepatocyte growth factor (HGF) [16]. Because of their potential clinical application, it has therefore become important to label the cells for tracing as transplanted cells.

Previous studies have shown that a cationic liposome (Lipofectamine) could transduce negatively charged QDs into ASCs within 4 h and the QDs remained in the cells for more than 2 weeks. However, cytotoxicity was observed at a relatively low concentration, suggesting that the major cause was the liposome (Lipofectamine) [17]. In this study, octa-arginine peptide (R8), which exhibits even greater efficiency in the delivery of several proteins, was utilized as a delivery vector and the characteristics of negatively charged carboxyl QDs transduced using R8 to live ASCs were investigated. In addition, imaging studies in subcutaneous transplantation on the back and intravenous transplantation through the tail vain were conducted.

2. Materials and methods

2.1. Animals

C57BL/6 mice were purchased from SLC Japan. The mice were housed in a controlled environment (12 h light/dark cycles at 21 °C) with free access to water and a standard chow diet before sacrifice. All conditions and handing of animals in this study were conducted with protocols approved by the Nagoya University Committee on Animal Use and Care.

2.2. Isolation and culture of ASCs

The 7–14-month-old female C57BL/6 mice were killed by cervical dislocation; adipose tissue specimens in the inguinal groove were isolated and washed extensively with Hank's balanced salt solution or phosphate-buffered saline (PBS) to remove the blood cells. The isolated adipose tissue specimens were cut finely and digested with 1 mL of 1 mg/mL typeIcollagenase (Collagenase TypeI, 274 U/mg, Koken Co., Ltd., Tokyo, Japan) at 37 °C in a shaking water bath for 45 min. The cells were filtrated using 250 μm nylon cell strainers (BD Biosciences) and suspended in Dulbecco's modified Eagle's medium and full-length name of F12 (DMEM/F12) containing 20% fetal bovine serum (FBS: Trace Scientific Ltd., Melbourne, Australia, Uin: 53141 Lot: B01249-500) and 100 U/ml penicillin/streptomycin (culture medium). They were centrifuged at 1200 rpm for 5 min at room temperature and adipose tissue-derived stem cells (ASCs) were obtained from the pellet. They were washed three times by suspension and centrifugation in culture medium and then were incubated overnight in culture medium at 37 °C with 5% CO_2. The primary cells were cultured for several days until they reached confluence and were defined as passage "0". The cells were used for the experiments between passages 2 and 5.

2.3. Preparation and transduction of R8-QDs complex

QDs (Invitrogen; Qdot ITK Carboxyl Quantum Dots) and R8 (Sigma genosys, Japan) were purchased. QDs were made from nanometer-scale crystals of a semiconductor material (CdSe), which are shelled with an additional semiconductor layer (ZnS) to improve their chemical and optical properties. In addition, the polymer coating has COO^- surface groups. To determine the optimal concentration ratio of QDs655 (emission at 655 nm)/R8 to transduce into ASCs, QDs655 (2.0 nM) and R8 were mixed for 20 min at room temperature in various ratios of QDs655/R8. Next, ASCs were incubated with the R8-QDs655 complex in a transduction medium (DMEM/F12, 2% FBS, 100 U/mL penicillin/streptomycin) at 37 °C. After 4 h incubation, the transduction efficiency of QDs655 into ASCs was evaluated by conventional fluorescence microscopy and a flow cytometry analysis [18].

2.4. Flow cytometry analysis

ASCs (1.5×10^5 cells) were seeded in 12-well plates (BD Biosciences) with 500 μL of culture medium for 2 h and the cells were transduced with QDs655 using R8 in transduction medium at 37 °C. After transduction, the cells were washed three times by suspension and centrifugation at 1200 rpm for 3 min. Next, the cells were suspended in 500 μL of PBS and used for flow cytometry analysis on a FACS caliber (BD Biosciences) flow cytometer using 488 nm laser excitation and 615 nm long pass emission.

2.5. Cytotoxicity of QDs to ASCs

The cells (2×10^4 cells) were seeded in 96-well plates (BD Biosciences) with 100 μL of culture medium for 2 h and then they were replaced with 100 μL of transduction medium at 37 °C. After 4 h incubation, QDs655 (0–24 nM) and R8 were mixed at the optimal ratio of $1{:}1 \times 10^4$, and ASCs were transduced with QDs655 using R8 in transduction medium for 24 h. Viable cells were counted using Cell Counting Kit-8 (CCK-8; DOJINDO Laboratories Kumamoto, Japan). CCK-8 reagent (10 μL) was added to each well and the reaction was allowed to proceed for up to 4 h. The absorbance of the sample at 450 nm was measured against a background control using a microplate reader.

2.6. Proliferation of ASCs labeled with QDs

ASCs (1×10^3 cells) were seeded in 96-well plate with 100 μL of culture medium and then transduced with QDs655 using R8 at various concentrations of QDs655 for 4 h. Next, the media was replaced with 100 μL of culture medium. After 0, 2, 4 and 5 days, viable cells were counted using the Cell Counting Kit-8 in the same way.

2.7. Confocal laser scanning microscopy

A confocal laser scanning microscopy (FV1000, OLYMPUS) analysis was conducted to confirm the fluorescent intensity and location of QDs655 in labeled ASCs using R8. Images obtained from the bottom of the coverslip to the top of the cells were recorded and each image was superimposed on PC to qualify the total brightness and pixel area of each region of interest. Before imaging, the cells were washed three times with PBS and replaced with fresh transduction medium [19].

2.8. Transduction of QDs using R8

ASCs were preincubated in the transduction medium with 10 mM sodium azide and 2-deoxy-D-glucose (endocytosis inhibitors) for 1 h at 37 °C, or 3 mM amiloride (macropinocytosis inhibitor) for 10 min at 37 °C. In addition, ASCs were preincubated in the transduction medium for 30 min at 4 °C (both endocytosis and macropinocytosis inhibitors). These cells were then washed three times with PBS followed by the addition of 0.4 nM QDs655 with R8 in fresh transduction medium for 1 h. Thereafter, the cells were observed using confocal laser scanning microscopy.

2.9. Adipogenic differentiation

Adipogenic differentiation was induced by culturing the cells for 3 days in DMEM (high glucose) containing 100 μM indometacin, 1 μM dexamethasone, 1 μM hydrocortisone, 10 μM insulin (Sigma, I-5500) and 10% FBS. The cells were then further cultured in DMEM (high glucose) containing 10% FBS for 2 weeks and the medium was changed every 3 days. Differentiation was confirmed by conventional microscopic observations of intracellular lipid droplets and Oil Red O staining as an indicator of intracellular lipid accumulation. Briefly, the cells were fixed in 10% solution of formaldehyde in PBS for at least 10 min at room temperature and then were washed with 60% isopropanol. Next, the cells were stained with 2% (w/v) Oil Red O reagent for 10 min at room temperature followed by repeated washing with distilled water and destaining in 100% isopropanol for 1 min.

2.10. Osteogenic differentiation

Osteogenic differentiation was induced by culturing the cells for 2 weeks in DMEM containing 200 μM dexamethasone, 50 μM ascorbate-2-phosphate (Wako Pure Chemical Industries Ltd., 013-12061), 10 mM α-glycerophosphate (Sigma, G-9891) and 10% FBS. The differentiation was confirmed by staining for any alkaline phosphatase activity and then observing the extracellular matrix calcification using Von Kossa's method. The cells were washed twice with PBS and fixed in 10% formalin for 15 min at room temperature. They were washed and incubated with deionized water for 15 min. Then, they were stained with a solution containing naphtol AS MX-PO_4 (Sigma, N-5000), *N,N*-dimethylformamide (Wako Pure Chemical Industries Ltd.), Red Violet LB salt (Sigma, F-1625) and Tris–HCl buffer (pH 8.3) for 45 min. Von Kossa staining was carried out with 2.5% silver nitrate solution for 30 min.

2.11. RNA extraction and real-time RT-PCR

Total RNA was extracted from cells by using RNeasy® reagent (QIAGEN) according to the manufacturer's instructions. cDNA synthesis and amplification via PCR were performed using Transcriptor High Fidelity cDNA Synthesis Kit (Roche Diagnostics GmbH, Mannheim, Germany). The cDNA was used for PCR by LightCycler® FastStart DNA Master PLUS SYBR Green I (Roche). The PCR reaction mixture was made up in 20 μL of 10 μM targeted gene oligonucleotides primers. Using LightCycler® (Roche), heat denaturation at 95 °C for 10 min and 40 cycles of PCR

Table 1
Primer sequences used for real-time RT-PCR.

Gene	Accession	Sense primer	Antisense primer
ALP	NM_007431	GTTGCCAAGCTGGGAGAACAC	CCCACCCCGCTATTCCAAAC
β-Actin	NM_007393	TATGGAATCCTGTGGCATCC	CTTCTGCATCCTGTCAGCAA

with denaturing at 95 °C for 10 s, annealing temperature 55 °C for 10 s and extension at 72 °C for 10 s were performed ALP and β-Actin. The sequences of all primers are shown in detail in Table 1.

2.12. In vivo fluorescent imaging of ASCs labeled with QDs

QDs655, QDs755 or QDs800 were transduced into ASCs using R8 in the same way. ASCs (0.5, 1 and 3 × 10^5 cells) labeled with QDs were subcutaneously transplanted with 50 μL PBS into the back of C57BL/6 mice. Images were taken using the Maestro *in vivo* imaging system (CRI Inc, Woburn, MA; excitation filter: 575–605 nm, emission filter: 645 nm long pass). The detection was set to capture images automatically at 10-nm increments from 630 nm to 850 nm with constant 1 s exposure. The resulting TIFF images were loaded into the vendor's software and analyzed.

On the other hand, for the *in vivo* imaging of ASCs transplanted into mouse through the tail vain, ASCs (5 × 10^5 cells) labeled with QDs800 were injected with 0.15 mL saline. Images were taken using the Maestro *in vivo* imaging system in the same way after 10 min. Moreover, for the histological analysis, ASCs (5 × 10^5 cells) labeled with QDs655 were injected into the mouse. The mouse was then sacrificed after 10 min and major organs (heart, lung, liver, spleen and kidney) were harvested and washed three times with PBS to remove retained erythrocytes. The collected tissue specimens were then fixed by formalin and embedded in paraffin. To examine the histological QDs uptake and distribution of transplanted ASCs, the tissue specimens were cut into 10 μm thick sections and then were observed by fluorescent microscopy.

2.13. Statistical analysis

Numerical values are presented as the mean ± SD. Each experiment was repeated three times. Statistical significance was evaluated using unpaired Student's *t*-test for comparisons between the two groups; *p*-values < 0.05 were considered to be statistically significant. All statistical analyses were performed using the SPSS software package.

3. Results

3.1. Transduction of QDs into ASCs using R8

QDs655 (2.0 nM) were mixed with concentrations of R8 (0, 0.2, 2.0, 20 and 200 μM) for 20 min respectively and they were tested for their ability to transduce into ASCs using conventional fluorescent microscopy and flow cytometry analysis. Red fluorescence derived from QDs655 was strongly observed at the ratio of 20 μM R8 to 2.0 nM QDs655. Increasing the R8 peptide concentration beyond 20 μM did not increase the QDs655 internalization. This result suggests that the concentration ratio of QDs:R8 of 1:1 × 10^4 is optimal for delivery into ASCs (Fig. 1A).

3.2. Cytotoxicity to ASCs

QDs655 was transduced into ASCs using R8 at various concentrations in transduction medium for 24 h at 37 °C. Significant cytotoxicity was observed in ASCs transduced with more than

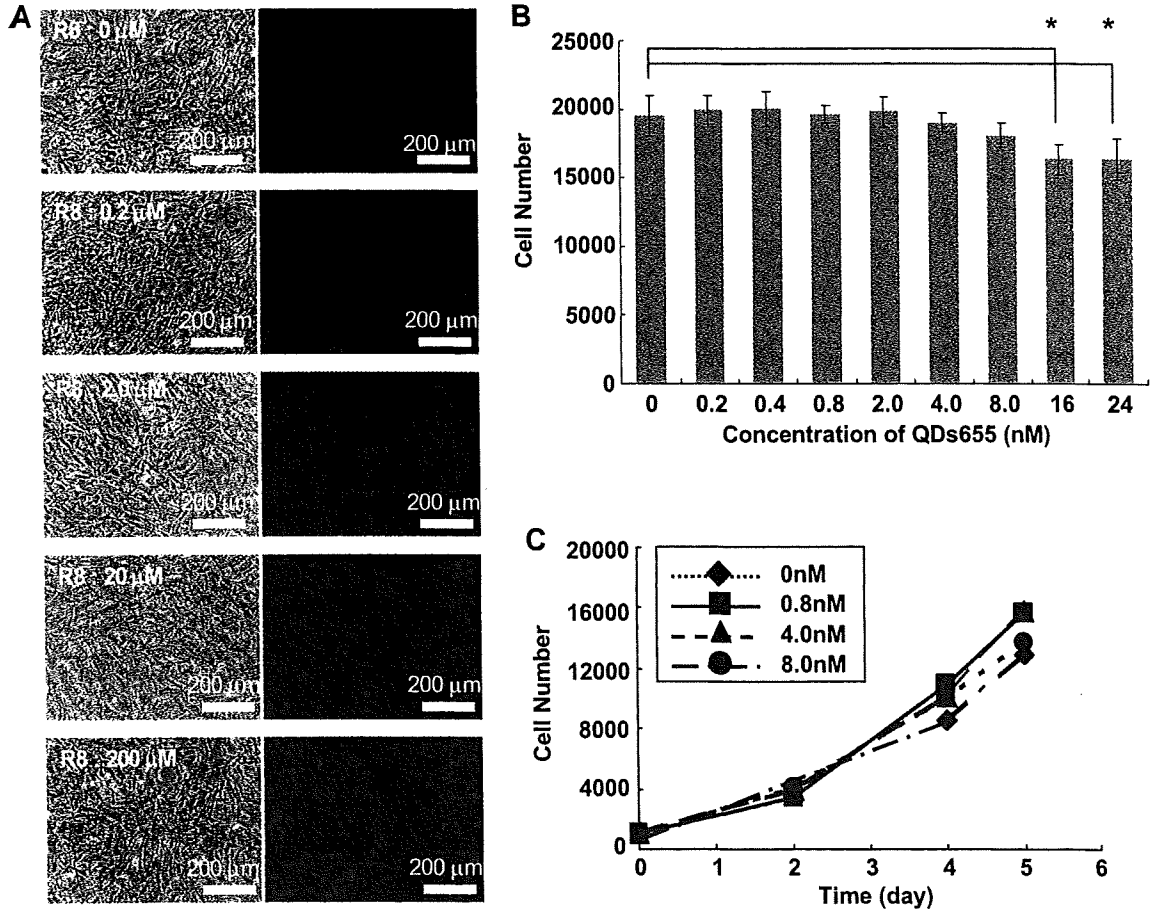

Fig. 1. Optimal formation of R8-QDs and the cytotoxicity to ASCs. A: QDs655 (2.0 nM) were mixed with various concentrations of R8 for 20 min and the complex were transduced into ASCs for 4 h to determine the optimal concentration ratio of QDs/R8. B: ASCs were transduced with QDs655 using R8 at various concentrations for 24 h. The survival of ASCs transduced with QDs655 using R8 is compared with non-transduction ASCs. C: The proliferation rate is shown in the nontoxic range of QDs655. The number of cells was estimated at 0, 2, 4, and 5 days after transduction as described in Materials and Methods. The data, all in triplicate, are shown as the mean ± SD values. *$p < 0.05$.

16 nM of QDs655, however, >80% of the cells were still alive. In addition, no remarkable cytotoxicity was observed with less than 8.0 nM of QDs655 (Fig. 1B). The morphology and fluorescent images were confirmed by conventional fluorescent microscopy.

Moreover, the influence on the proliferation rate was examined within the non-cytotoxic range of concentrations. The cells were confirmed to exhibit a logarithmic growth rate that was nearly equal to normal ASCs. There were no significant differences in these concentrations (Fig. 1C). These data suggest that ASCs could be labeled within an 8.0 nM concentration of QDs using R8.

3.3. Transduction efficiency of QDs using R8

To determine the transduction efficiency of QDs into ASCs, ASCs were transduced with QDs655 using R8 for 1 h at 0, 0.8, 2.0 and 8.0 nM concentrations of QDs655. The internalization of QDs655 was estimated and compared using flow cytometry analysis. The transduction efficiency of QDs655 after 1 h transduction was 81.4 ± 5.4% at 0.8 nM, 90.8 ± 2.8% at 2.0 nM and 95.2 ± 1.9% at 8.0 nM (Fig. 2A). More than 80% of the cells could be labeled within 1 h (Fig. 2B).

In addition, the location and fluorescent intensity of QDs655 was analyzed using confocal laser scanning microscopy at a concentration of 0.4 nM QDs655 after 1 h of transduction. The successive location of QDs655 in the ASCs was observed in 1 h, 8 h, 1 day, 7 days, 10 days and 14 days after transduction. QDs655 were widely dispersed in the cell cytoplasm during the early time points, however, aggregation of QDs655 was observed as time passed, QDs655 could not be observed in the nuclei at any time (Fig. 3A). The fluorescent intensity level of QDs655 was approximately equal during 14 days (Fig. 3B).

3.4. Transduction of QDs using R8 by macropinocytosis

The internalization of QDs655 using R8 with sodium azide and 2-deoxy-D-glucose, or amiloride, or at 4 °C was compared to that of normal transduction. The fluorescence of QDs655 could be observed on the face of the ASCs only and not in the cytoplasm (Fig. 4A–C). On the other hand, QDs655 were incorporated into the cytoplasm of ASCs after no application of inhibitors (Fig. 4D). These results suggested that the internalization of QDs655 using R8 occurs mainly by macropinocytosis.

3.5. Differentiation of ASCs transduced with QDs using R8

To examine the influence on the pluripotency of ASCs, ASCs were transduced with 0.4 nM of QDs655 using R8 and cultured with adipogenic and osteogenic medium for 2 weeks. Following adipogenic differentiation, intracellular lipid droplets in ASCs labeled with QDs655 were observed in the same frequency as the control ASCs and the red fluorescence derived from internalized QDs655 was confirmed (Fig. 5A-a). Oil Red O staining confirmed that intracellular droplets were lipid (data not shown). On the other hand, after incubation in osteogenic medium, ASCs labeled with QDs655 became osteocyte-like in morphology with cuboidal shapes (Fig. 5A-b). The cells were positive for von Kossa's staining in the same frequency as the control ASCs (data not shown). Red fluorescence of QDs655 was clearly observed for more than 2 weeks using confocal laser scanning microscopy in both of the differentiated cell types. However, the fluorescence of QDs655 was only slightly observed in the ASCs cultured with normal culture medium (Fig. 5A-c).

Moreover, to estimate the influence on osteogenic differentiation ability of ASCs at the mRNA revel, ALP activity was measured by real-time RT-PCR. ALP activity of ASCs transduced with QDs655

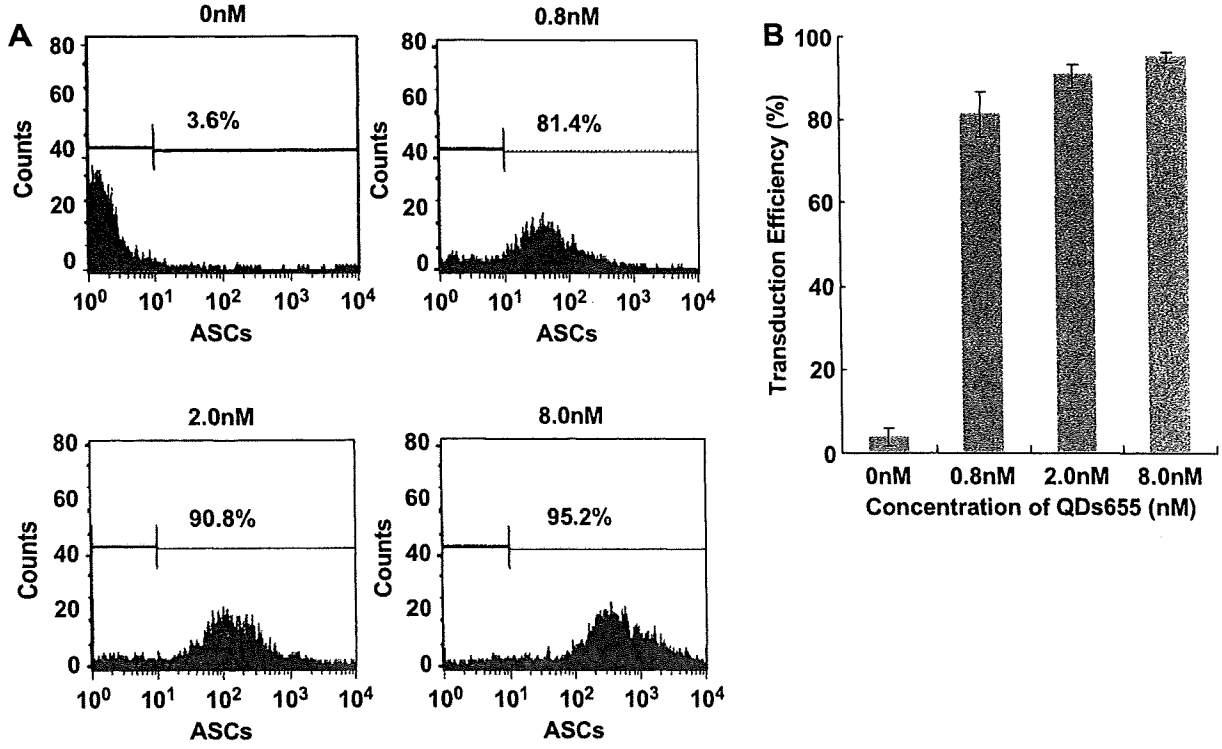

Fig. 2. Transduction efficiency of QDs using R8 quantified by flow cytometry. A: The transduction efficiency of QDs655 into ASCs using R8 after 1 h of incubation was quantified by flow cytometry. The mean fluorescent units are the average of 10,000 units. B: The bar graph shows the transduction efficiency of QDs655 using R8 after 1 h of transduction.

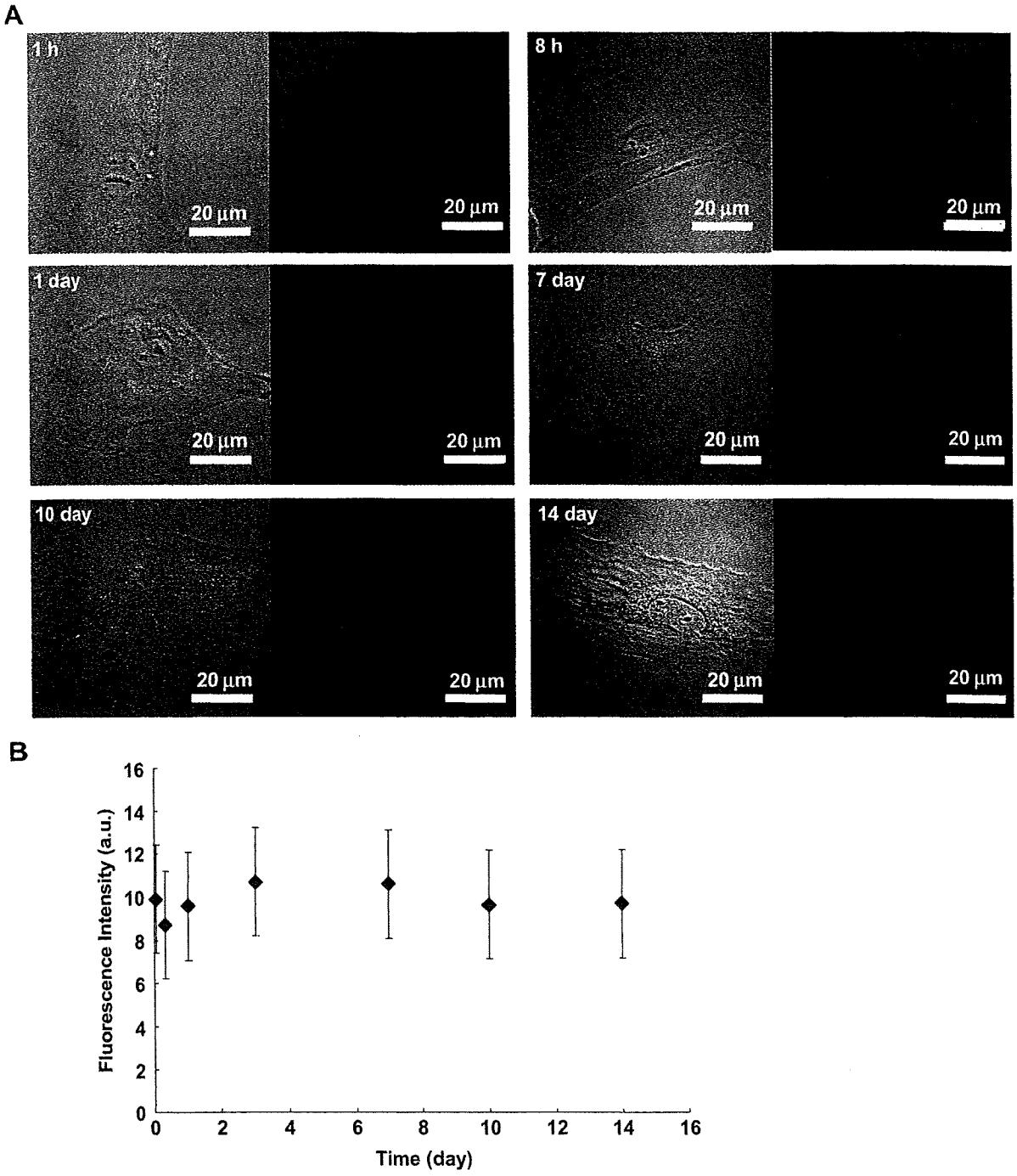

Fig. 3. Intracellular distribution and fluorescence intensity of QDs. A: The intracellular distribution of QDs655 in 1 h, 8 h, 1 day, 7 days, 10 days and 14 days after transduction were obtained by confocal laser scanning microscopy. Internalized QDs655 are shown by the red fluorescence. B: The fluorescence intensity was measured by confocal laser scanning microscopy. The data, in each triplicate, are shown as the mean ± SD values.

using R8 in osteogenic differentiation was observed at the same level as that of the non-transduced ASCs (Fig. 5B and C). These data suggested that the differentiation ability of ASCs was not inhibited by QDs655 transduction using R8.

3.6. Detection sensitivity for in vivo imaging

ASCs (0.5×10^5, 1.0×10^5 and 3.0×10^5 cells) labeled with QDs655 using R8 were injected subcutaneously with saline into the back of the mice. The Maestro Optical Imaging System (excitation filter: 575–605 nm, emission filter: 645 nm long pass) was used to observe the mice 1 h after transplantation. Moreover, images were obtained 1, 2, 5 and 7 days after transplantation (Fig. 6A) and the intensity was evaluated (Fig. 6B). The results suggested that ASCs labeled with QDs655 could be detected up to 7 days following subcutaneous transplantation.

On the other hand, one of the advantages of QDs is their ability for multiplex imaging. Multiplex imaging may be applied for

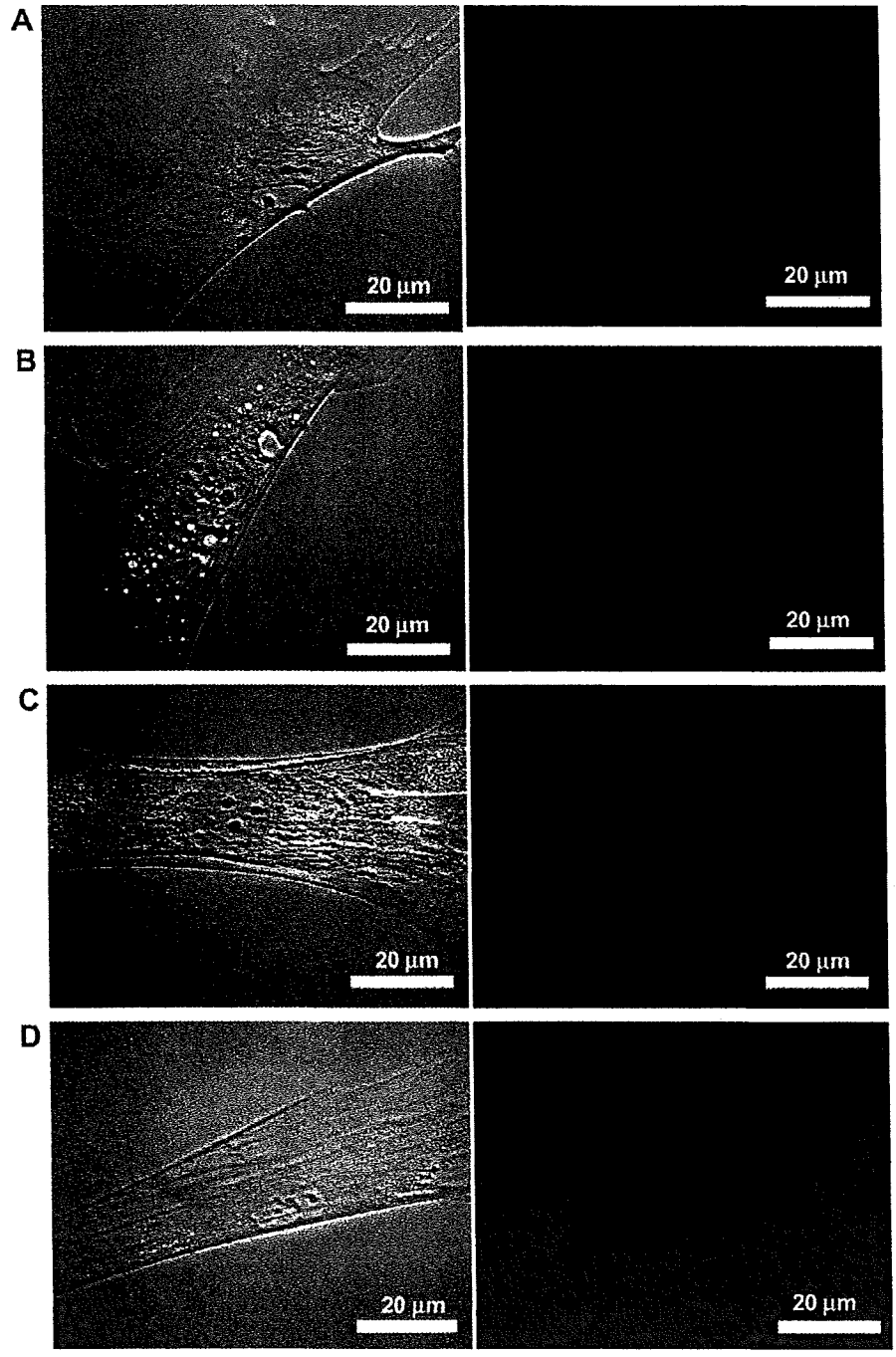

Fig. 4. Transduction mechanism of QDs using R8 into ASCs. A: ASCs were preincubated in the transduction medium with 10 mM sodium azide and 2-deoxy-D-glucose (endocytosis inhibitors) for 1 h at 37 °C. B: ASCs were preincubated in the transduction medium with 3 mM amiloride (macropinocytosis inhibitor) for 10 min at 37 °C. C: ASCs were preincubated in the transduction medium for 30 min at 4 °C (both endocytosis and macropinocytosis inhibitors). These cells were washed three times with PBS followed by addition of 0.4 nM QDs655 using R8 in the fresh transduction medium for 1 h. D: ASCs were incubated with 0.4 nM QDs655 with R8 under the normal transduction condition. These cells were observed using confocal laser scanning microscopy.

tracing different cell populations at the same time. Almost all kinds of QDs can be excited by the same wavelength and a different wavelength of light is emitted depending on the size of the QDs. In this study, ASCs (1×10^5 cells) were labeled with QDs655, 705 and 800 using R8 respectively and subcutaneously transplanted into the back of the mice and the multiplex image in 1 h was obtained in 1 h after transplantation (Fig. 6C).

Furthermore, ASCs labeled with QDs800 using R8 were transplanted through the tail vein of a mouse to examine whether the fluorescence of QDs800 from the ASCs could be detected and demonstrate the distribution of transplanted ASCs. When the mouse was sacrifice after 10 min, the fluorescence of QDs800 could be detected in the lung only by the Maestro *in vivo* imaging system (Fig. 7A). On the other hand, a histological analysis showed that the

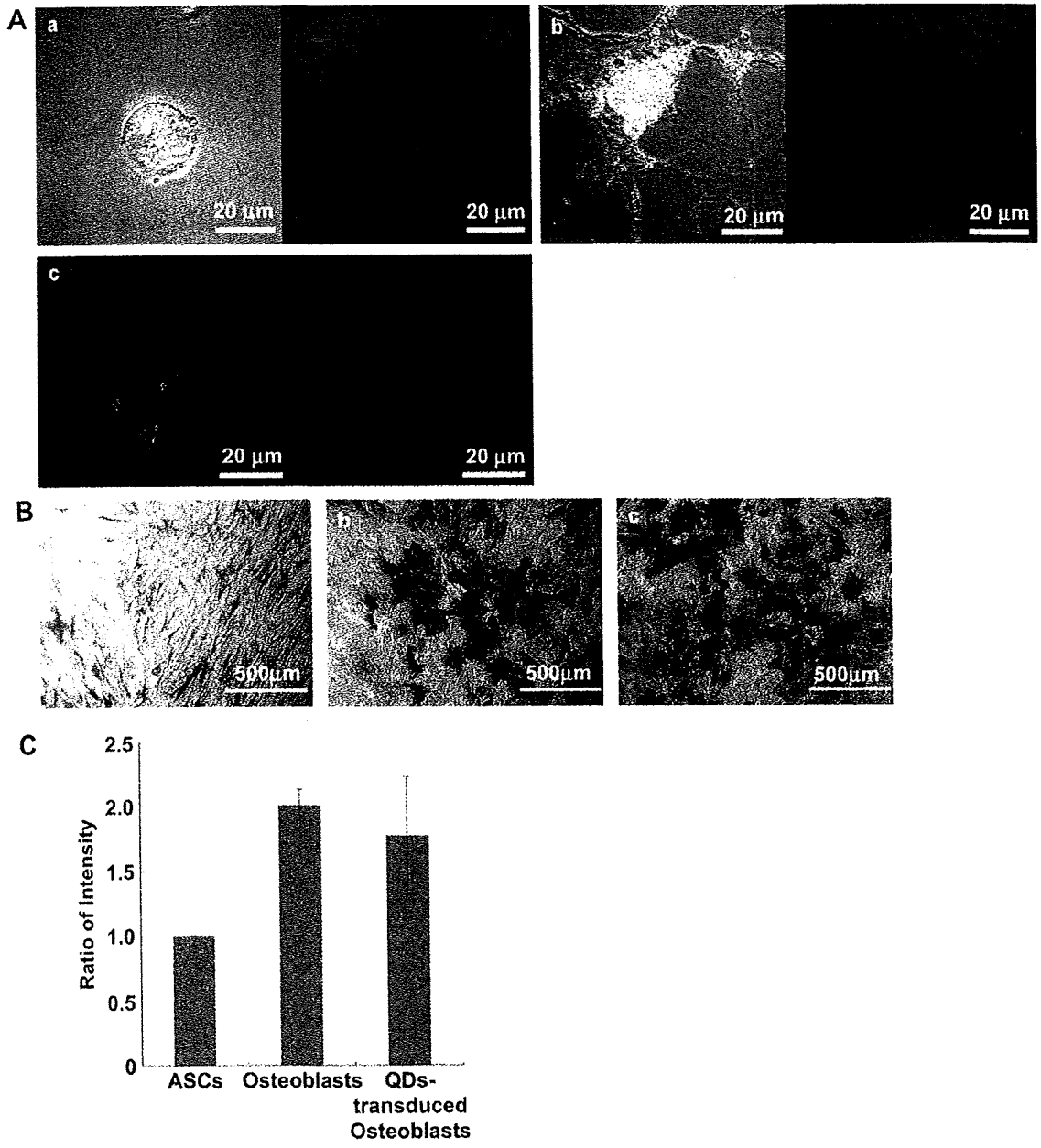

Fig. 5. Differentiation of ASCs transduced with QDs using R8. A: ASCs transduced with QDs655 (0.4 nM) using R8 were differentiated to lipocytes (a) or osteocytes (b) for 2 weeks. ASCs transduced with QDs655 (0.4 nM) using R8 were incubated in the culture medium without differentiation (c). These figures were obtained using confocal laser scanning microscopy. Phase contrast (left) and QDs655 fluorescent (right) were shown. B: Negative ALP staining of normal cultured (non-differentiated) ASCs (a), positive ALP staining of osteogenic induced ASCs (b) and osteogenic induced ASCs transduced with QDs655 using R8 (c) were confirmed. C: The quantification of ALP mRNA levels was compared in three groups. There was no significant difference between non-transduced ASCs and ASCs transduced with QDs655 using R8 ($p > 0.05$), but significantly more ALP activity was expressed than in the control ASCs ($p < 0.05$).

presence of ASCs could be confirmed in slices of the lungs only using conventional fluorescent microscopy (Fig. 7C). The heart and kidney data were not shown.

4. Discussion

Several studies have reported that some cells could passively internalize QDs in the culture medium without carrier or microinjection, electroporation and liposome-based transduction [7,11]. ASCs could not be transduced with QDs only without the help of carriers (data not shown). A cationic liposome "Lipofectamine" was used for the transduction of QDs into ASCs without further modification [17]. However, cytotoxicity was observed at a comparatively low concentration of >2.0 nM. In addition, the transduction time was relatively long (4 h at 0.8 nM of QDs655). Recently, CPPs mediated transduction has attracted more and more attention for the efficient cellular membrane delivery and labeling [12,20,21].

R8 which exhibits even greater efficiency in the delivery of several proteins was employed in order to overcome these problems. Moreover, compared with other articles [4,7,8], the transduction efficiency of R8 seems to be similar to CLO-Tat, CHPNH2 and pep-1. On the other hand, the molecular length of R8 is shorter

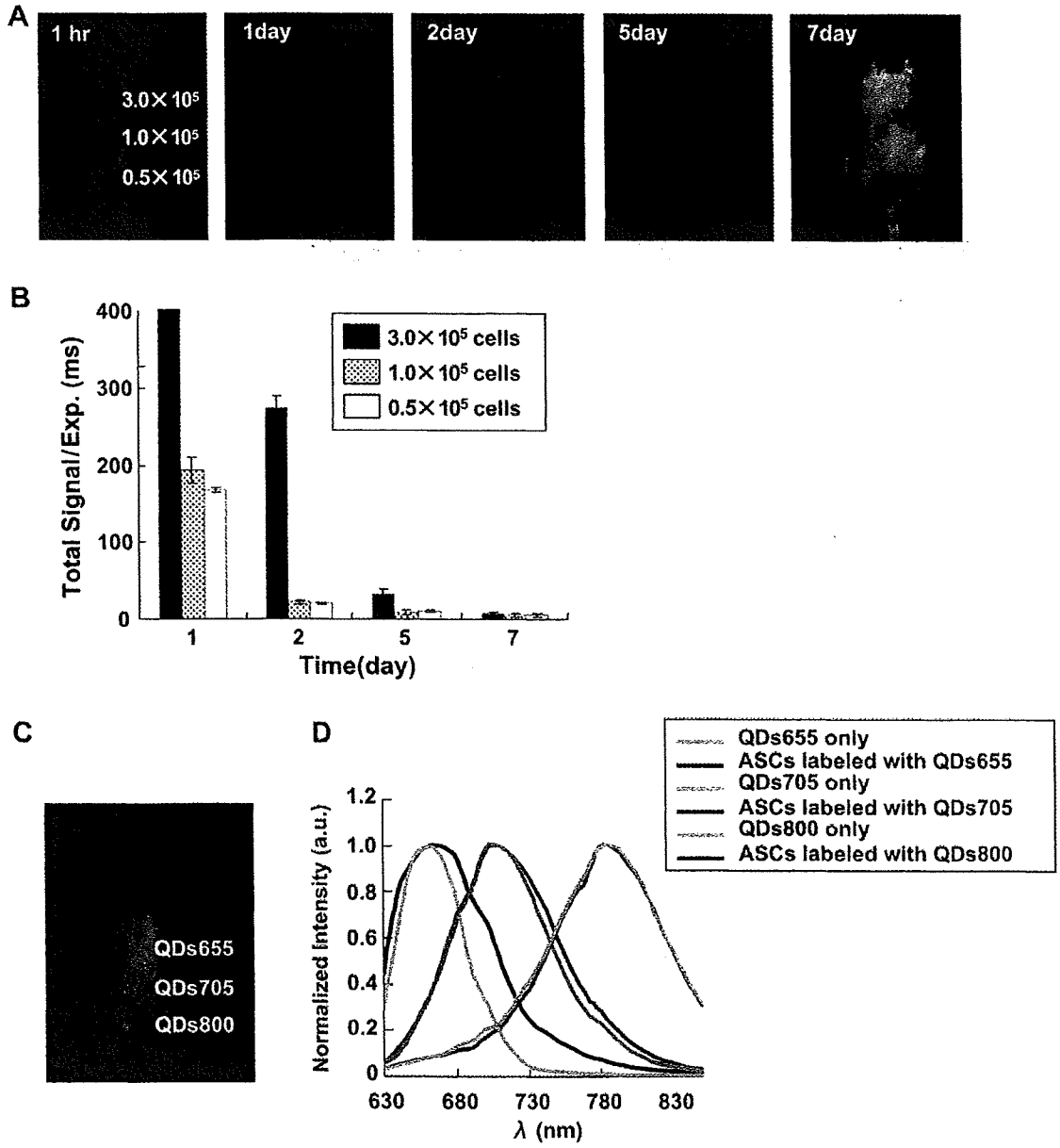

Fig. 6. Detection and multiplex imaging capability of QDs in subcutaneous transplantation. A: ASCs (0.5×10^5, 1.0×10^5 and 3.0×10^5 cells) labeled with QDs655 (0.8 nM) using R8 were subcutaneously transplanted into the backs of the mice. These images were taken 1 h, 1, 2, 5 and 7 days past injection (excitation filter 575–605 nm, emission filter 645 nm long pass). B: The bar graph shows the change of fluorescence intensity of QDs655 for 7 days at the number of ASCs labeled with QDs655. C: ASCs (1.0×10^5 cells) labeled with QDs655, 705 and 800 were subcutaneously injected on the back of the mice. The image was taken 10 min after transplantation with a single excitation light source. D: The graph was the fluorescent spectra of ASCs labeled with QDs655, QDs705 and QDs800.

than the others, thus the cost of synthesis is lower than the others. The cytotoxicity was greatly reduced by using R8. No cytotoxicity was observed in ASCs transduced with less than 16 nM of QDs655, and no drastic decrease in the number of cells was observed with more than 8.0 nM of QDs655. These results suggested that the effect of internalized QDs on the cell cytotoxicity was dependent on surface coating rather than on the total amount of internalized QDs. Furthermore, as observed in a previous report, the current results indicate that ASCs labeled with QDs using R8 had no adverse effects on cell proliferation, measured by the CCK-8 assay [7]. On the other hand, the QDs transduction mechanism using R8 into ASCs was investigated by incubation at 4 °C, with inhibitors of endocytosis, such as sodium azide, and macropinocytosis, such as amiloride (Fig. 4). The QDs internalization was suppressed by these inhibitors, thus suggesting that the transduction of QDs into ASCs occurred through macropinocytosis.

The transduction time and maintenance of stem cell potency after transduction of QDs are very important, when QDs are employed clinically for regenerative medicine. In this study, the fluorescence intensity of internalized QDs reached almost its peak by 1 h. The transduction time of QDs using R8 was markedly decreased in comparison to Lipofectamine [17]. On the other hand, the CPPs delivery of QDs rescued the cells from the negative effects caused by the internalized QDs to osteogenic and chondrogenic-associated lineage markers [7]. ASCs transduced with QDs655 using R8 cultured with adipogenic and osteogenic

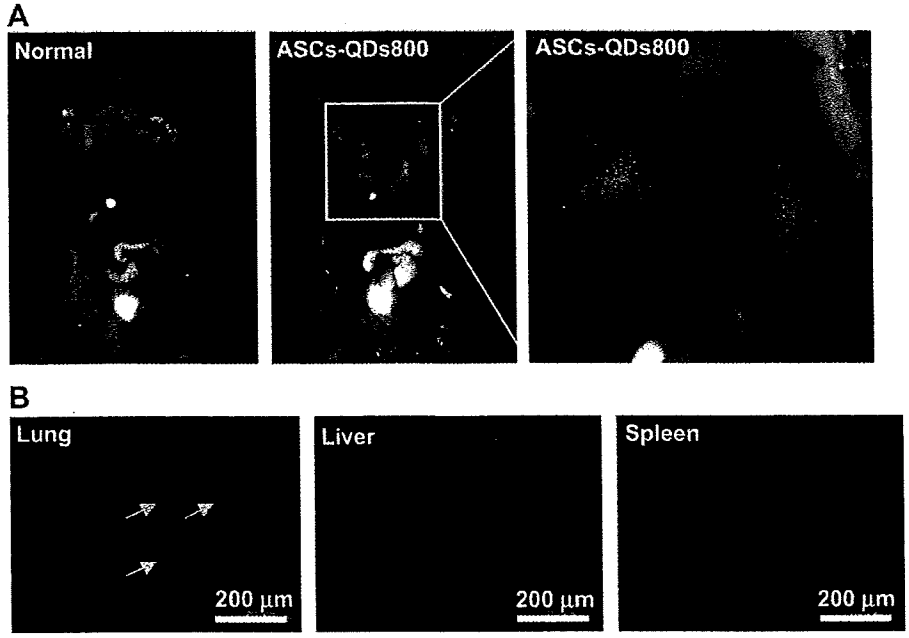

Fig. 7. *In vivo* imaging of ASCs labeled with QDs after intravenous injection. A: ASCs (5.0×10^5 cells) labeled with QDs800 (0.8 nM) using R8 were transplanted through the tail vain into mouse. The images were taken 10 min after injection (excitation filter 575–605 nm, emission filter 645 nm long pass). B: The red fluorescence of QDs655 was detected in the lung only, with little or no QDs655 accumulation in the liver or spleen.

medium for 2 weeks differentiated into adipogenic and osteogenic cells, respectively, in the current study. ALP activity of ASCs transduced with QDs655 using R8 following osteogenic differentiation was exhibited at the same level as that for the non-transduced ASCs. Moreover, Jui-Chih Chang et al. checked the influence to the cell surface of ASCs with QDs using cell-penetrating peptide (CPP). In mesenchymal stem cells (MSCs), cell surface receptors such as CD29, CD44, CD73, CD90, CD105, etc. are accredited the prototypical markers. According to the reference, it was found that CPP delivery preserved CD29, CD44, CD73, CD90 and CD105 expressions [7]. These data suggested that ASCs transduced with QDs using R8 maintained their stem cell potency. However, Jui-Chih Chang et al. reported that Pep-1, a CPP, coated QDs, affected the gap junctions of human mesenchymal stem cell [13]. It will be necessary to ascertain the influence of R8 on gap junctions of ASCs in future studies. The fluorescence intensity in differentiated ASCs transduced with QDs655 was sustained at least for 2 weeks. On the other hand, undifferentiated ASCs transduced with QDs655 in the culture medium, showed markedly reduced fluorescence intensity after 2 weeks of culture. The differences may be due to their proliferative activity [5]. However, the QDs655 signal was confirmed, thus suggesting that QDs could be available for labeling of ASCs for 2 weeks.

QDs exhibit several advantages in comparison to conventional organic labels, such as a high luminance, resistance to photobleaching, a range of excitation wavelengths and narrow emission bandwidths. Therefore, QDs have a potential application for *in vivo* imaging. ASCs labeled with QDs655 using R8 were subcutaneously injected with saline into the backs of the mice. ASCs labeled with QDs655 could be detected up to 7 days following subcutaneous transplantation, but the fluorescence intensities were drastically decreased. This reduction might be due to the rapid division of ASCs as suggested in a previous report [22]. When the ASCs labeled with QDs655 were incubated with DMEM/F12 mediun containing 2% FBS, the fluorescence of QDs was maintained for 2 weeks at almost the same label. This result was suggested that internalized QDs were diluted by cell proliferation in the culture medium and incorporated into the cytoplasm of ASCs after escape from the lysosome fraction system [23]. Another advantage of QDs is their ability to for multiplex imaging of different QDs at the same time [22]. When ASCs transduced with QDs655, 705 and 800 respectively were transplanted into the back of mouse subcutaneously at the different points, their fluorescence of all three species could be observed at the same time 1 h after transplantation.

On the other hand, QDs fluorescence below the wavelength range 650 nm was not used often for sensitive imaging of deeper tissues in recent papers [22,24,25]. Deep tissue imaging (millimeters to centimeters) requires the use of far red and near infrared light in the spectral range 650–900 nm [26], because these regions eliminated overlap with major absorption peaks of blood and water *in vivo*. When ASCs labeled with QDs800 were transplanted through the tail vein into a mouse, the fluorescence could be detected in the lung. ASCs labeled with QDs655 and 705 could not be observed *in vivo* because of the strong autofluorescence of liver tissue. Besides, it was reported that QDs fluorescence could be detected in other organs such as the liver and spleen in other papers [12]. In this study, mice were killed 10 min after ASCs transplantation and this suggested that almost all ASCs stayed in the lung. Therefore, i.v. ASCs transplantation may be useful treatment modality for lung disease in the future [24].

As for the fate of QDs using R8 *in vivo*, Neera V. Gopee et al. showed that when QDs were injected intradermally (ID) on the right dorsal flank of the female SFH-1 hairless mice, the QDs could be observed moving from the injection sites apparently through the lymphatic duct system to regional lymph nodes within minutes. Residual QDs remained at the site of injection until necropsy at 24 h. Moreover, using inductivity coupled plasma mass spectrometry (ICP-MS), showed accumulation in the liver, regional draining lymph nodes, kidney, spleen, and hepatic lymph node [27].

On the other hand, Hak Soo Choi et al. showed that when QDs leaked into the vascular in the intravenously injection, the QDs were accumulated in the liver. And then, the QDs were transported to the kidney and cleared by urinary excretion [28].

5. Conclusion

ASCs possess the ability of self-renewing and differentiating into various mesenchymal cell types. Because of their potential clinical application, it has therefore become important to label the cells for tracing as transplanted cells. The concentration ratio of QDs:R8 of $1:1 \times 10^4$ was optimal for delivery into ASCs and the cells could be labeled within an 8.0 nM concentration of QDs using R8. In addition, ASCs could be labeled within about 1 h and the fluorescent intensity level of QDs was during 14 days at least. The differentiation ability of ASCs was not inhibited by QDs transduction using R8. Moreover, ASCs labeled with QDs could be detected following subcutaneous transplantation and injection through tail vein *in vivo*. This study suggested that QDs labeling using R8 could be utilized for the imaging of ASCs.

Acknowledgements

This work was supported by the Kobayashi Pharmaceutical Company. We thank Miwa Natsume, Takafumi Kinoshita and Rio Fujita for technical advice, and Yukiko Masuda, Nagisa Otake and Sumiko Nishio (Nagoya University) for their assistance.

Appendix

Figures with essential color discrimination. All figures of this article are difficult to interpret in black and white. The full color images can be found in the on-line version, at doi:10.1016/j.biomaterials.2010.01.134.

References

[1] Seleverstov O, Zabirnyk O, Zscharnack M, Bulavina L, Nowicki M, Heinrich JM, et al. Quantum dots for human mesenchymal stem cells labeling. A size-dependent autophagy activation. Nano Lett 2006;6(12):2826–32.
[2] Zhang T, Stilwell JL, Gerion D, Ding L, Elboudwarej O, Cooke PA, et al. Cellular effect of high doses of silica-coated quantum dot profiled with high throughput gene expression analysis and high content cellomics measurements. Nano Lett 2006;6(4):800–8.
[3] Zhang Y, He J, Wang PN, Chen JY, Lu ZJ, Lu DR, et al. Time-dependent photoluminescence blue shift of the quantum dots in living cells: effect of oxidation by singlet oxygen. J Am Chem Soc 2006;128(41):13396–401.
[4] Hsieh SC, Wang FF, Lin CS, Chen YJ, Hung SC, Wang YJ. The inhibition of osteogenesis with human bone marrow mesenchymal stem cells by CdSe/ZnS quantum dot labels. Biomaterials 2006;27(8):1656–64.
[5] Hoshino A, Hanaki K, Suzuki K, Yamamoto K. Applications of T-lymphoma labeled with fluorescent quantum dots to cell tracing markers in mouse body. Biochem Biophys Res Commun 2004;314(1):46–53.
[6] Jaiswal JK, Mattoussi H, Mauro JM, Simon SM. Long-term multiple color imaging of live cells using quantum dot bioconjugates. Nat Biotechnol 2003;21(1):47–51.
[7] Chang JC, Su HL, Hsu SH. The use of peptide-delivery to protect human adipose-derived adult stem cells from damage caused by the internalization of quantum dots. Biomaterials 2008;29(7):925–36.
[8] Ohyabu Y, Kaul Z, Yoshioka T, Inoue K, Sakai S, Mishima H, et al. Stable and nondisruptive *in vitro*/*in vivo* labeling of mesenchymal stem cells by internalizing quantum dots. Hum Gene Ther 2009;20(3):217–24.
[9] Toita S, Hasegawa U, Koga H, Sekiya I, Muneta T, Akiyoshi K. Protein-conjugated quantum dots effectively delivered into living cells by a cationic nanogel. J Nanosci Nanotechnol 2008;8(5):2279–85.
[10] Shah B, Clark P, Stroscio M, Mao J. Labeling and imaging of human mesenchymal stem cells with quantum dot bioconjugates during proliferation and osteogenic differentiation in long term. Conf Proc IEEE Eng Med Biol Soc 2006;1:1470–3.
[11] Lagerholm BC. Peptide-mediated intracellular delivery of quantum dots. Methods Mol Biol 2007;374:105–12.
[12] Lei Y, Tang H, Yao L, Yu R, Feng M, Zou B. Applications of mesenchymal stem cells labeled with Tat peptide conjugated quantum dots to cell tracking in mouse body. Bioconjug Chem 2008;19(2):421–7.
[13] Chang JC, Hsu SH, Su HL. The regulation of the gap junction of human mesenchymal stem cells through the internalization of quantum dots. Biomaterials 2009;30(10):1937–46.
[14] Shah BS, Clark PA, Moioli EK, Stroscio MA, Mao JJ. Labeling of mesenchymal stem cells by bioconjugated quantum dots. Nano Lett 2007;7(10):3071–9.
[15] Yukawa H, Noguchi H, Oishi K, Miyazaki T, Kitagawa Y, Inoue M, et al. Recombinant sendai virus-mediated gene transfer to adipose tissue-derived stem cells (ASCs). Cell Transplant 2008;17(1–2):43–50.
[16] Yukawa H, Noguchi H, Oishi K, Takagi S, Hamaguchi M, Hamajima N, et al. Cell transplantation of adipose tissue-derived stem cells in combination with heparin attenuated acute liver failure in mice. Cell Transplant 2009;18(5):601–9.
[17] Yukawa H, Mizufune S, Mamori C, Kagami Y, Oishi K, Kaji N, et al. Quantum dots for labeling adipose tissue-derived stem cells. Cell Transplant 2009;18(5):591–9.
[18] Mattheakis LC, Dias JM, Choi YJ, Gong J, Bruchez MP, Liu J, et al. Optical coding of mammalian cells using semiconductor quantum dots. Anal Biochem 2004;327(2):200–8.
[19] Akita H, Ito R, Khalil IA, Futaki S, Harashima H. Quantitative three-dimensional analysis of the intracellular trafficking of plasmid DNA transfected by a nonviral gene delivery system using confocal laser scanning microscopy. Mol Ther 2004;9(3):443–51.
[20] Zhao M, Kircher MF, Josephson L, Weissleder R. Differential conjugation of tat peptide to superparamagnetic nanoparticles and its effect on cellular uptake. Bioconjug Chem 2002;13(4):840–4.
[21] Lewin M, Carlesso N, Tung CH, Tang XW, Cory D, Scadden DT, et al. Tat peptide-derivatized magnetic nanoparticles allow *in vivo* tracking and recovery of progenitor cells. Nat Biotechnol 2000;18(4):410–4.
[22] Lin S, Xie X, Patel MR, Yang YH, Li Z, Cao F, et al. Quantum dot imaging for embryonic stem cells. BMC Biotechnol 2007;7:67.
[23] Mudhakir D, Akita H, Khalil IA, Futaki S, Harashima H. Pharmacokinetic analysis of the tissue distribution of octa-arginine modified liposomes in mice. Drug Metab Pharmacokinet 2005;20(4):275–81.
[24] Suzuki H, Hogg JC, van Eeden SF. Sequestration and homing of bone marrow-derived lineage negative progenitor cells in the lung during pneumococcal pneumonia. Respir Res 2008;9:25.
[25] So MK, Xu C, Loening AM, Gambhir SS, Rao J. Self-illuminating quantum dot conjugates for *in vivo* imaging. Nat Biotechnol 2006;24(3):339–43.
[26] Gao X, Cui Y, Levenson RM, Chung LW, Nie S. *In vivo* cancer targeting and imaging with semiconductor quantum dots. Nat Biotechnol 2004;22(8):969–76.
[27] Gopee NV, Roberts DW, Webb P, Cozart CR, Siitonen PH, Warbritton AR, et al. Migration of intradermally injected quantum dots to sentinel organs in mice. Toxicol Sci 2007;98(1):249–57.
[28] Choi HS, Liu W, Misra P, Tanaka E, Zimmer JP, Itty Ipe B, et al. Renal clearance of quantum dots. Nat Biotechnol 2007;10:1165–70.

Biology of Neurodegeneration

Neuro-degenerative Diseases

Neurodegenerative Dis 2010;7:64–67
DOI: 10.1159/000285508

Published online: February 18, 2010

Neuroprotective and Neurotoxic Phenotypes of Activated Microglia in Neonatal Mice with Respective MPTP- and Ethanol-Induced Brain Injury

Hirohide Sawada[a, b] Hiromi Suzuki[c] Toshiharu Nagatsu[b, c] Makoto Sawada[c]

[a]Department of Medical Technology, Kobe Tokiwa University, Kobe, [b]School of Medicine, Fujita Health University, Toyoake, and [c]Research Institute of Environmental Medicine, Nagoya University, Nagoya, Japan

Key Words
Microglia · Neonatal mice · Ethanol · 1-Methyl-4-phenyl-1,2,3,6-tetrahydropyridine

Abstract
Activated microglia play important roles in the inflammatory process and progression in Parkinson's disease. These cells produce various cytokines, nitric oxide, and neurotrophins, which are pleiotropic in their action, i.e., neuroprotective or neurotoxic. In an in vivo study on a mouse model with nigrostriatal lesions produced by the administration of 1-methyl-4-phenyl-1,2,3,6-tetrahydropyridine (MPTP), microglia activated by systemic lipopolysaccharide (LPS) were neurotoxic toward dopamine neurons in aged mice, but unexpectedly, neuroprotective in neonatal mice. In contrast to microglia in the MPTP model, LPS-activated microglia in neonatal mice in a model made by the stereotaxic injection of ethanol into the striatum were neurotoxic, and systemic LPS administration in the ethanol-injury model caused marked increases both in the volume of necrotic lesions and in the number of degenerative neurons in the striatum. Thus, activated microglia in the neonatal mouse brain play either a neuroprotective or neurotoxic role depending on the type of brain injury.

Introduction

Microglia play important roles in inflammatory processes in various neurodegenerative diseases including Parkinson's disease (PD). Activated microglia play either a neuroprotective or neurotoxic role by producing pro-inflammatory cytokines [e.g., tumor necrosis factor-α (TNF-α), interleukin-1β (IL-1β), nitric oxide (NO), reactive oxygen species (ROS)], or neurotrophic factors [e.g., nerve growth factor (NGF), brain-derived neurotrophic factor (BDNF), glial cell line-derived neurotrophic factor (GDNF)]. Sawada et al. [1] separated two subsets of microglia from mouse brain based on their capacity for intracellular ROS production stimulated by phorbol-12-myristate-13-acetate (PMA): one cell line was neurotoxic when cocultured with neurons and had a high capacity for ROS production, whereas the other cell line was neuroprotective and showed no ROS production. On the other hand, it is well known that neonatal microglia are very proliferative and easily activated under normal circumstances compared with adult microglia [2, 3]. Thus, a question arises as to whether or not activated neonatal microglia are different from those in adult or aged cells in terms of neuroprotective or neurotoxic phenotypes.

KARGER
Fax +41 61306 12 34
E-Mail karger@karger.ch
www.karger.com

1660–2854/10/0073–0064$26.00/0

Accessible online at:
www.karger.com/ndd

Hirohide Sawada
Department of Medical Technology, Kobe Tokiwa University
2-6-2 Ohtani-cho, Nagata-ku
Kobe, Hyogo 653-0838 (Japan)
Tel. +81 78 611 1821, Fax +81 78 643 4361, E-Mail h-sawada@kobe-tokiwa.ac.jp

Table 1. Effects of LPS-induced activated microglia in mouse models with MPTP- or ethanol-induced neurodegeneration

Model	Toxin administration	Toxin + LPS administration
Neonatal mice (P7) treated with MPTP	Decreased DA neuron numbers in SN Decreased DA and DOPAC levels in midbrain Normal IL-1β and IL-6 levels in midbrain	Normal DA neuron numbers in SN Increased TH activity, DA and DOPAC levels in midbrain Increased IL-1β and IL-6 levels in midbrain
Neonatal mice (P7) treated with ethanol	Moderate decrease in number of striatal neurons in striatum	Severe decrease in number of striatal neurons in striatum
Aged mice (60 weeks) treated with MPTP	Moderate decrease in number of DA neurons in SN	Severe decrease in number of DA neurons in SN

SN = Substantia nigra; TH = tyrosine hydroxylase.

Neuroprotective Phenotype of Microglia Activated by Lipopolysaccharide in Neonatal Mice with MPTP-Induced Injury

Many reports on postmortem PD brains and PD animal models indicate that activated microglia have neurotoxic effects and may play a significant role in progression of the disease. Also aging is thought to be an important factor in idiopathic PD [4]. Aging may promote the toxic change from the protective to the toxic phenotype of activated microglia, as hypothesized by Sawada et al. [1]. This hypothesis of a toxic change in activated microglia had its origin in the in vitro experiments conducted by Vilhardt et al. [5]. Sawada et al. [6] showed in neonatal and aged mice different phenotypes of microglia activated by systemic lipopolysaccharide (LPS) treatment on dopamine (DA) neurons under 1-methyl-4-phenyl-1,2,3,6-tetrahydropyridine (MPTP)-induced injury (table 1). MPTP is a chemical that causes PD-like symptoms in humans and various animals. Although the number of DA neurons in the substantia nigra in aged mice treated with MPTP was significantly decreased, an increase in the number of LPS-activated microglia produced a further decrease in the number of these neurons. By contrast, neonatal (postnatal day 7) mice treated with MPTP showed that the initial decrease in the levels of DA neurons, tyrosine hydroxylase activity, DA, and the metabolite 3,4-dihydroxyphenylacetic acid in the midbrain changed to an increase, along with marked LPS-induced activation of microglia and increased levels of pro-inflammatory cytokines of IL-1β and IL-6. These results suggest that LPS-activated microglia in neonatal mice may have neurotrophic potential. Imai et al. [7] also showed the neuroprotective effects of exogenously administered microglia isolated from neonatal gerbils in an ischemic gerbil model; the exogenous microglia migrated to ischemic hippocampal regions in the host, and enhanced neuroprotection accompanied by the expression of neurotrophic factors BDNF and GDNF.

Neurotoxic Phenotype of Microglia Activated by LPS in Neonatal Mice with Local Ethanol Injury

Sawada et al. [manuscript in preparation] examined whether or not LPS-activated neonatal microglia also show the neuroprotective phenotype in an ethanol-induced brain injury model [8–10] produced by the stereotaxic injection of 100% ethanol (2 μl) into the mouse striatum. This local injection of ethanol produced more severe neuronal damage than seen in the MPTP-induced PD model. This ethanol-induced model produced brain injury without hemorrhage, infection or other unexpected effects that might affect the cytokine networks in the brain. After the ethanol-induced damage, activated microglia accumulated in the boundary area of the necrosis and eliminated damaged neurons by causing delayed neuronal death. A large lesion with a necrotic core was observed in the ethanol-injected striatum, and activated microglia had migrated to the outside of this necrotic mass, where Fluoro-Jade B (FJB)-positive degenerative neurons were observed. By previous treatment with systemic LPS or saline as a control, the volumes of necrotic and degenerative areas in the striatum were further increased along with an in-

crease in the number of activated microglia (table 1). The number of inducible NO-synthesizing enzyme (iNOS)-positive microglia also tended to be increased by the LPS treatment, suggesting NO as a toxic agent. These results suggest that LPS-activated microglia in the neonatal mouse striatum play a neurotoxic role in the ethanol-induced brain injury.

The Mechanisms of Neuroprotective and Neurotoxic Phenotypes of Neonatal Microglia

The mechanisms responsible for the difference in the phenotypes of activated neonatal microglia between the MPTP- and ethanol-injury models remains to be further examined. Neonatal microglia are activated by macrophage colony-stimulating factor (MCSF) from late gestation to 2 weeks, and are very proliferative and easily activated under normal circumstances. As described above, LPS-activated microglia in the neonatal MPTP model showed a neuroprotective phenotype in the substantia nigra, but a neurotoxic phenotype was observed in neonatal mice that received ethanol-induced striatal damage. In the MPTP model, elevated levels of IL-1β and IL-6 in the midbrain were observed, which suggests that these pleiotropic cytokines produced by activated neonatal microglia may have neuroprotective consequences. As a hypothesis, LPS-activated microglia in the ethanol-injury mouse model might be only transiently neuroprotective, rapidly converting to the neurotoxic phenotype that secretes toxic molecules such as NO. Inoue [11] reviewed microglial activation by ATP and ADP released from injured neurons. At low concentrations of ATP, microglia release neurotrophic substances such as plasminogen, TNF-α, and IL-6. Stronger or longer stimulation with ATP induced iNOS synthesis in microglia with high concentrations of NO to cause neuronal death. Thus, a high concentration or long-time exposure to extracellular ATP may change the phenotype from protective to toxic.

Since ethanol itself has been shown to influence microglial activation [12–16], the influence of ethanol on microglial activation by local administration might be different depending on the dose, duration, and timing of exposure. Thus the combined effects of LPS with ethanol on microglial activation may also augment the neurotoxic phenotype. Chronic exposure to ethanol was reported to cause increased production of superoxide anion in cultured neonatal hamster microglia; a similar increase was not seen during acute ethanol exposure [13].

Although the limitations of the local ethanol-injury model should be carefully considered, this model has advantages for examining the protective or toxic mechanisms of activated microglia in a specific brain region at any age. Further studies on the molecules secreted from the LPS-activated microglia around the area injured by ethanol should provide valuable information on mechanisms of neurodegeneration.

Acknowledgements

This work was supported by grants from the Ministry of Health, Labor, and Welfare of Japan (M.S.), the Ministry of Education, Culture, Sports, Science, and Technology of Japan (M.S.), and the Japan Health Sciences Foundation (M.S.).

References

1 Sawada M, Imamura K, Nagatsu T: Role of cytokines in inflammatory process in Parkinson's disease. J Neural Transm 2006; 70(suppl):373–381.

2 Sawada M, Suzumura A, Yamamoto H, Marunouchi T: Activation and proliferation of the isolated microglia by colony stimulating factor-1 and possible involvement of protein kinase C. Brain Res 1990;509:119–124.

3 Thery C, Hetier E, Evrard C, Mallat M: Expression of macrophage colony-stimulating factor gene in the mouse brain during development. J Neurosci Res 1990;26:129–133.

4 Sawada M, Sawada H, Nagatsu T: Effects of aging on neuroprotective and neurotoxic properties of microglia in neurodegenerative diseases. Neurodegenerative Dis 2008;5: 254–256.

5 Vilhardt F, Plastre O, Sawada M, Suzuki K, Wiznerowicz M, Kiyokawa E, Trono D, Krause KH: The HIV-1 Nef protein and phagocyte NADPH oxidase activation. J Biol Chem 2002;277:42136–42143.

6 Sawada H, Hishida R, Hirata Y, Ono K, Suzuki H, Muramatsu S, Nakano I, Nagatsu T, Sawada M: Activated microglia affect the nigro-striatal dopamine neurons differently in neonatal and aged mice treated with 1-methyl-4-phenyl-1,2,3,6-tetrahydropyridine. J Neurosci Res 2007;85:1752–1761.

7 Imai F, Suzuki H, Oda J, Ninomiya T, Ono K, Sano H, Sawada M: Neuroprotective effects of exogenous microglia in global brain ischemia. J Cereb Blood Flow Metab 2007;27:488–500.
8 Takeuchi A, Isobe K, Miyaishi O, Sawada M, Fan ZH, Nakashima I, Kiuchi K: Microglial NO induces delayed neuronal death following acute injury in the striatum. Eur J Neurosci 1998;10:1613–1620.
9 Takeuchi A, Miyaishi O, Kiuchi K, Isobe K: Cu/Zn- and Mn-superoxide dismutases are specifically up-regulated in neurons after focal brain injury. J Neurobiol 2000;45:39–46.
10 Toyama H, Hatano K, Suzuki H, Ichise M, Momosaki M, Kudo G, Ito F, Kato T, Yamaguch H, Katada K, Sawada M, Ito K: In vivo imaging of microglial activation using a peripheral benzodiazepine receptor ligand: [11C]PK-11195 and animal PET following ethanol injury in rat striatum. Ann Nucl Med 2008;22:417–424.
11 Inoue K: Microglial activation by purines and pyrimidines. Glia 2002;40:156–163.
12 Qin L, He J, Hanes RN, Pluzarev O, Hong JS, Crews FT: Increased systemic and brain cytokine production and neuroinflammation by endotoxin following ethanol treatment. J Neuroinflammation 2008;5:10.
13 Colton CA, Snell-Callanan J, Chernyshev ON: Ethanol induced changes in superoxide anion and nitric oxide in cultured microglia. Alcohol Clin Exp Res 1998;22:710–716.
14 Aroor AR, Baker RC: Ethanol inhibition of phagocytosis and superoxide anion production by microglia. Alcohol 1998;15:277–280.
15 Lee H, Jeong J, Son E, Mosa A, Cho GJ, Choi WS, Ha JH, Kim IK, Lee MG, Kim CY, Suk K: Ethanol selectively modulates inflammatory activation signaling of brain microglia. J Neuroimmunol 2004;156:88–95.
16 Suk K: Microglial signal transduction as a target of alcohol action in the brain. Curr Neurovasc Res 2007;4:131–142.

Neuroscience Letters 473 (2010) 146–150

Contents lists available at ScienceDirect

Neuroscience Letters

journal homepage: www.elsevier.com/locate/neulet

Delayed neural damage is induced by iNOS-expressing microglia in a brain injury model

Kenji Ono*, Hiromi Suzuki, Makoto Sawada

Department of Brain Functions, Division of Stress Adaptation and Protection, Research Institute of Environmental Medicine, Nagoya University, Nagoya, Aichi 464-8601, Japan

ARTICLE INFO

Article history:
Received 18 January 2010
Received in revised form 12 February 2010
Accepted 13 February 2010

Keywords:
Brain injury
Neurotoxicity
Nitric oxide
iNOS
Microglia

ABSTRACT

Most CNS diseases begin with inflammation with subsequent neural damage eventually occurring; however, the process leading from the onset of inflammation to neural damage remains obscure. We used an artificial brain injury mouse model and examined how neural damage occurred in the brain parenchyma. The damaged area in each mouse was clearly observed by magnetic resonance imaging (MRI), and the progression of damage was observed to occur in a biphasic manner (acute damage, within 1 week; delayed damage, after 2 weeks). We found that the delayed neural damage was absent in iNOS-deficient mice (iNOS-KO mice). Then, we analyzed brain tissues and determined that delayed neural damage was accompanied by an increase in the levels of NO end products and iNOS expression, with accumulation of iNOS-expressing microglia around the injured area. In addition, the expression of IL-1β mRNA was increased in areas affected by acute damage, but not in those affected by delayed damage. These findings suggest that delayed neural damage might arise from NO production by iNOS-expressing activated microglia and that such activated microglia might become a therapeutic target for many CNS diseases.

Many diseases of the central nervous system (CNS), such as brain injury, infection, inflammation, ischemia, trauma, brain tumors, and neurodegenerative diseases, are associated with neural damage. CNS diseases are often accompanied by inflammatory responses, including microglial activation leading to increased phagocytic activity, secretion of pro-inflammatory cytokines, and NO and ROS production; these eventually lead to neural damage. Therefore, many brain diseases are triggered by inflammatory responses/microglial activation prior to the occurrence of severe tissue damage; however, the process leading from the onset of inflammation to neural damage remains obscure.

Neural damage due to diseases are often related to nitric oxide (NO) [10] and reactive oxygen species (ROS) [7]. One of the responses to cerebral ischemia is an increase in the production of NO [6], and synergistic neurotoxicity in a Parkinson's disease model was shown to be involved in the production of NO and ROS [4]. NO is produced by many cells in the brain including neurons, astrocytes, microglia, and endothelial cells, and acts as a neurotransmitter under physiological conditions [5]. In contrast, in CNS diseases, NO production is increased and NO becomes a neurotoxic mediator. Therefore, neural damage might arise from NO production in CNS diseases accompanied by inflammation. In brain, although NO is biosynthesized by two types of nitric oxide synthase (NOS), constitutive NOS and inducible NOS, the latter is mainly induced in microglia, astrocytes, and invasive macrophages around sites of inflammation, and the concentration of NO markedly increases around such sites [2,23]. Moreover, NO production and release via iNOS induction cause neuronal damage around sites of inflammation [1], such that metabolites of NO might be appropriate for use as an index of exacerbation around inflammation.

An artificial brain injury model produced by a stereotaxic injection of ethanol into striatum is known to exhibit neural cell damage accompanied by microglial activation but without migration of inflammatory cells from the bloodstream [21,22]. As a feature of this model, activated endogenous microglia accumulate around the injured area and express iNOS, which results in an increase in the level of NO at the injured site [21]. To clarify the processes behind the damage caused by brain injury, imaging techniques for use on living animals, such as MRI, can provide useful information regarding the severity of neural damage at an injured area. In MRI, T1-weighted images are useful in investigating anatomical structure and T2-weighted images are effective in finding lesion sites in brains by increasing signal intensities [13].

In this study, we produced an artificial brain injury model via ethanol injection with normal and iNOS-knockout mice and examined how neural damage occurred in the brain parenchyma after brain injury by MRI, and histochemical and biochemical analyses.

Each C57BL/6 mouse or iNOS-KO mouse ([B6.129P2-Nos2<tmILau>/J], The Jackson Laboratories, ME) was anesthetized and placed in a stereotactic frame, and the skull was exposed. 1 mm burr holes were drilled and the following coordinates were used to position a 10 μl Hamilton syringe: the needle was placed

* Corresponding author. Tel.: +81 52 789 5002; fax: +81 52 789 3994.
E-mail address: k_ono@riem.nagoya-u.ac.jp (K. Ono).

0304-3940/$ – see front matter © 2010 Elsevier Ireland Ltd. All rights reserved.
doi:10.1016/j.neulet.2010.02.041

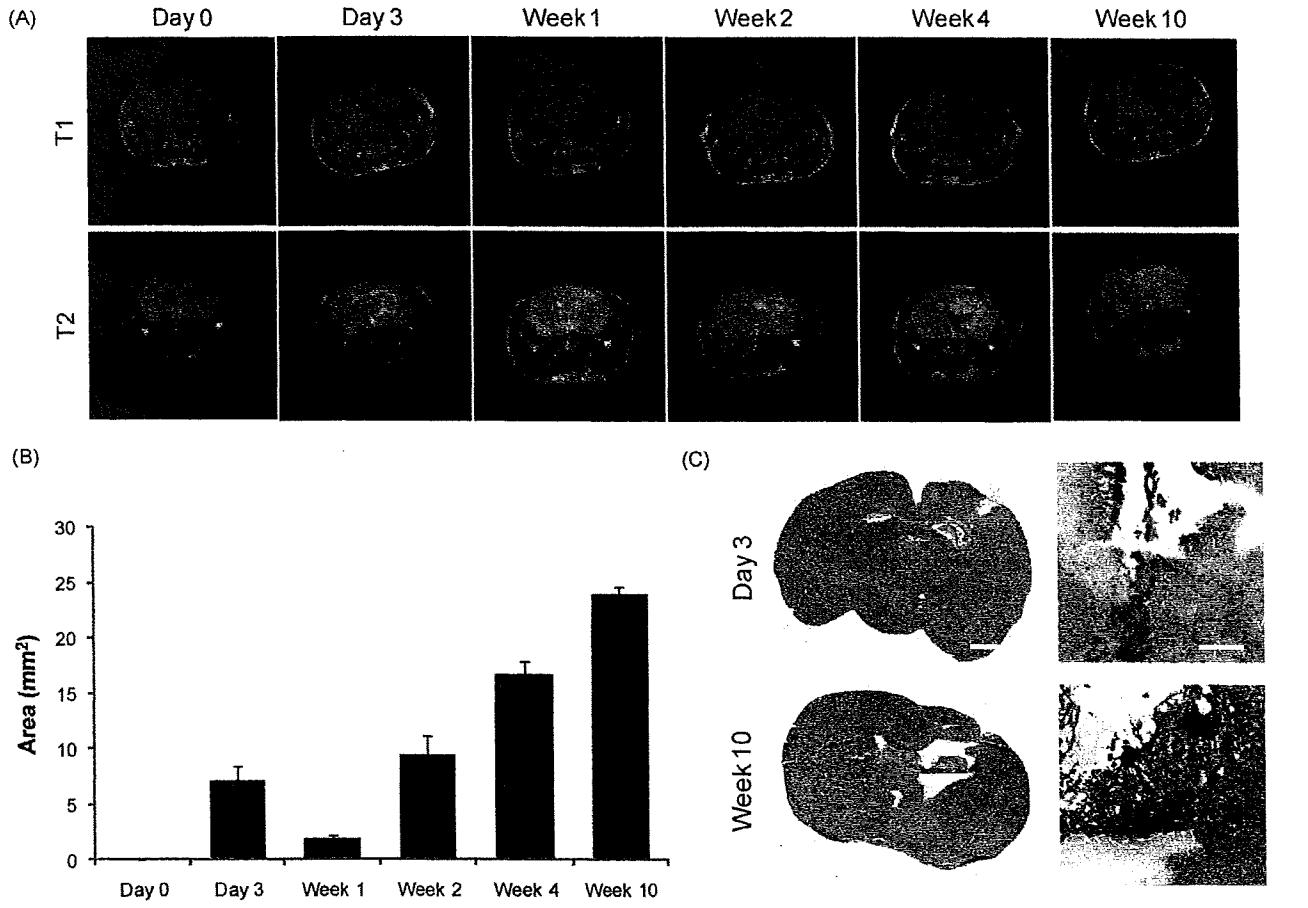

Fig. 1. Progression of neural damage after brain injury in normal mice (A) T1-weighted (T1) and T2-weighted (T2) images of each mouse before and during 10 weeks after brain injury were obtained by MRI. (B) This graph indicates the injured area observed in T2-weighted images obtained before and after brain injury. Values represent the mean ± SD. (C) These photographs show brain sections after HE staining at 3 days and 10 weeks after brain injury. The photographs on the right show magnified images of the injured area shown to the left. Each scale bar in left and right photographs indicates 2 mm and 100 μm, respectively.

4.0 mm anterior to the bregma, 4.0 mm lateral to the midline, and 3.5 mm ventral to the cortical surface to deliver cells to the striatum. At each site, an injection volume of 5 μl of ethanol (EtOH) was delivered at a rate of 1 μl/min, and the needle was withdrawn after an additional 5 min. At 3 days, 1, 2, 4, and 10 weeks, the hearts of anesthetized mice were perfused with about 100 ml of isotonic saline, and then each brain was isolated, frozen in liquid nitrogen, and embedded in OCT compound (Tissue Tek; Miles, Elkhart, IN).

MRI was sequentially performed on the treated mice. Each mouse was anesthetized with 1.0% isoflurane and held in an MRI coil. It was set in MRI equipment (MRTechnology, Inc., Tsukuba, Japan) and serial T1-weighted and T2-weighted images were acquired in accordance with the manufacturer's instructions. The acquired T2-weighted images were analyzed in terms of signal intensity using Photoshop CS2 software and the area (mm^2) of neural damage was calculated.

Brain sections (10 μm) were serially cut with a cryostat microtome (Leica Microsystems K.K., Japan), then transferred to MAS-coated slides (Matsunami Glass Ind., Ltd., Japan) and air-dried. The sections were fixed with 4% paraformaldehyde in PBS at 4 °C for 15 min and treated with 0.1% triton-X for improvement of permeability. The sections were multiply labeled with monoclonal antibodies against Mac-1 (a murine complement component C3bi receptor marker; BMA, Switzerland) and inducible nitric oxide synthase (iNOS; BD Biosciences, Tokyo, Japan). The reaction was visualized with Cy3-conjugated goat anti-rat IgG (Jackson Immunoresearch Laboratories, Inc., PA) at a dilution of 1:400 and Alexa350-conjugated goat anti-mouse IgG (Invitrogen, Carlsbad, CA) at a dilution of 1:200. Some sections were also subjected to hematoxylin–eosin (HE) staining for confirmation of morphological changes. Fluorescent images were captured with an imaging system (Apotome; Carl Zeiss, Tokyo, Japan) and HE images were captured with Aperio ScanScope system (Aperio Technology, CA).

The accumulation of nitrite and nitrate in the brain was measured as described previously [11]. In brief, 20 slices of brain sections (10 μm) were homogenized in TNE buffer (10 mM Tris–HCl, pH 7.5, 1% NP-40, 0.15 M NaCl, 1 mM EDTA), centrifuged at 13,000 rpm for 30 min at 4 °C for 15 min, and supernatant fractions were collected. The supernatants were centrifuged at 7000 × g with a filter (Ultrafree-MC microcentrifuge device, Millipore, Tokyo, Japan) to remove substances larger than 10 kDa. The filtrates were analyzed using a NO_2/NO_3 Assay Kit-C II (Dojindo, Kumamoto, Japan). After nitrate was reduced to nitrite by nitrate reductase, the absorbance at 595 nm was measured after reaction with Griess reagent. The obtained value was expressed as the total of NO end products, nitrite and nitrate. Nitrite and nitrate were expressed in micromolar concentrations based on tissue weight. Total RNA was extracted from 40 serial brain sections (10 μm/slice) using RNeasy mini kit and RNase-free DNase set (QIAGEN, Hilden, Germany) in accordance with the manufacturer's instructions. RNA (1 μg) was reverse-transcribed at 37 °C for 90 min in a mixture containing 100 U recombinant M-MLV reverse transcriptase, 0.1 μg DNA random hexamers, 40 U RNase inhibitor, and 1.4 mM dNTPs, in a final volume of 50 μl. The cDNA was amplified and analyzed

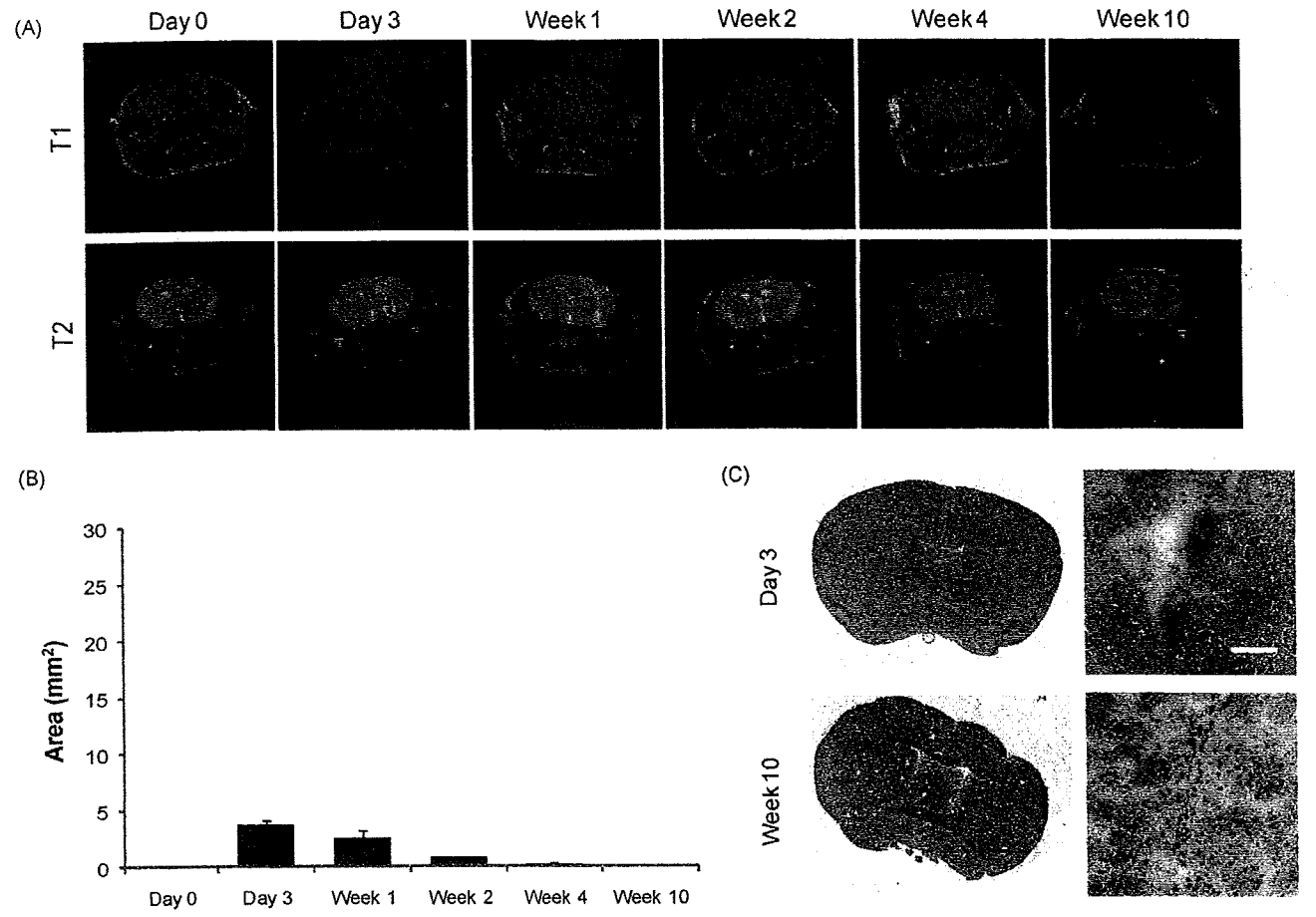

Fig. 2. Progression of neural damage in late phase was not observed in iNOS-KO mice (A) T1-weighted (T1) and T2-weighted (T2) images of each iNOS-KO mouse before and during 10 weeks after brain injury were obtained by MRI. (B) This graph indicates the injured area observed in T2-weighted images of iNOS-KO mice obtained before and after brain injury. Values represent the mean ± SD. (C) These photographs show brain sections after HE staining at 3 days and 10 weeks after brain injury. The photographs on the right show magnified images of the injured area to the left. Each scale bar in left and right photographs indicates 2 mm and 100 μm, respectively.

with Power SYBR Green PCR Master Mix and 7900 Real-Time PCR System (Applied Biosystems, Tokyo, Japan) using primer pairs specific to iNOS (sense primer: GCA GCT ACT GGG TCA AAG ACA A; antisense primer: TCT CTG CCT ATC CGT CTC GTC), IL-1β (sense primer: CGT GGA CCT TCC AGG ATG AG; antisense primer: GGA GCC TGT AGT GCA GCT GTC), or glyceraldehyde-3-phosphate dehydrogenase (GAPDH; sense primer: TGC ACC ACC AAC TGC TTA G; antisense primer: GAT GCA GGG ATG ATG TTC) for 40 cycles (95 °C for 15 s, 60 °C for 60 s). Expression of iNOS and IL-1β mRNA was analyzed by the Delta–Delta Ct method [3].

To estimate the severity of injury in the brain of living animals by MRI, T1-weighted and T2-weighted images from each normal C57BL/6 mouse before and after the brain injury were examined (Fig. 1A), since T1-weighted images are generally useful in investigating anatomical structures and T2-weighted images are effective in finding lesion sites in tissues by increasing the signal intensity. The damaged area was clearly observed by MRI and the progression of damage was found to occur in a biphasic manner (Fig. 1B). The first damage occurred within 1 week (acute damage), and subsequent damage occurred more than 2 weeks after the brain injury (delayed damage). To confirm individual neural damage histologically, brain sections were analyzed by hematoxylin–eosin (HE) staining (Fig. 1C). As observed by MRI, HE staining also indicated slight destruction of brain tissue in the acute damage phase and severe destruction in the delayed damage phase. The accumulation of many infiltrating cells was observed around the injured area in the delayed damage phase. Neural damage that occurred owing to the artificial brain injury was also investigated in iNOS-KO mouse by MRI (Fig. 2A). Similar acute damage to that in normal mice was observed; however, delayed damage was not observed in either T1-weighted or T2-weighted images (Fig. 2A and B). HE staining indicated that in the acute phase a similar extent of tissue destruction occurred to that in the normal mouse; however, no tissue destruction was observed in the delayed phase for the iNOS-KO mouse (Fig. 2C). Then, the amount of NO end products was measured in the brain tissues of normal and iNOS-KO mice by the Griess method (Fig. 3A). NO end products were detected in uninjured brains of both normal and iNOS-KO mice; their levels were significantly lower in iNOS-KO mice than in normal mice. In normal mice, the level of NO end products increased slightly but significantly at 3 days then further increased at 2 weeks after the injury up to about 2-fold that in the uninjured brain. In contrast, the levels of NO end products in brains in iNOS-KO mice at 3 days after the injury were unchanged and their levels hardly increased at 2 weeks after the injury. The expression of iNOS was analyzed by quantitative PCR (Fig. 3B). The expression of iNOS mRNA increased in a biphasic manner in the injured hemisphere of normal mouse brain. The expression of iNOS mRNA increased 2.5-fold in the acute phase and 6-fold in the delayed phase. Immunohistochemical analysis with antibodies against Mac-1 and iNOS indicated that the activated form of microglia expressed iNOS in brain sections of both acute and delayed phases (Fig. 3C). At 3 days after the brain injury, some of the microglia cells around the injured area expressed iNOS. They showed round and ameboid forms and were dispersed. At 4

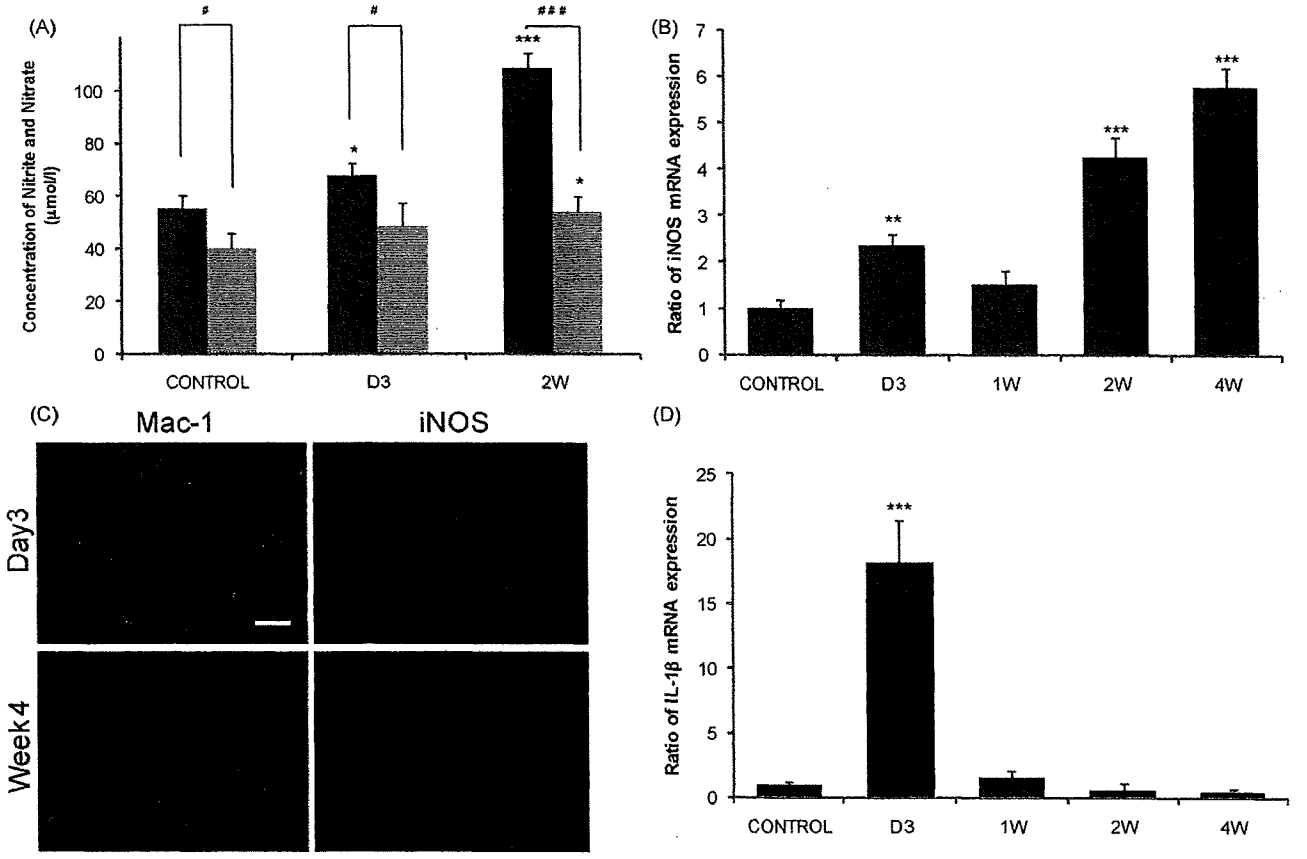

Fig. 3. Microglia produced NO via iNOS expression in delayed neural damage after brain injury. (A) The concentrations of total NO end products at 3 days and 2 weeks after brain injury were analyzed by the Griess method. Dark gray bars indicate normal mice and light gray bars indicate iNOS-KO mice. (B) This graph indicates the expression of iNOS mRNA in the brain during 4 weeks after brain injury. (C) These photographs show brain sections at 3 days and 4 weeks after brain injury. The photographs on the left indicate Mac-1 staining and those on the right indicate iNOS staining. Photographs on the same row indicate the same location. The scale bar indicates 100 μm. (D) This graph indicates the expression of IL-1β mRNA in the brain during 4 weeks after brain injury. CONTROL, mice without brain injury; D3, mice at 3 days after brain injury; 1W, mice at 1 week after brain injury; 2W, mice at 2 weeks after brain injury; 4W, mice at 4 weeks after brain injury. Values represent the mean ± SD. $^{*}P<0.05$, $^{**}P<0.01$, $^{***}P<0.001$ vs. CONTROL and $^{\#}P<0.05$, $^{\#\#\#}P<0.001$ vs. normal mice before and after brain injury using Student's *t*-test.

weeks after the brain injury, most of the microglia cells around injured areas expressed iNOS. They showed branched forms as well as ameboid forms and most of them accumulated near the injured site. To determine the state of microglial activation, the expression of IL-1β was analyzed by quantitative PCR (Fig. 3D). The expression of IL-1β mRNA in the injured hemisphere of the brain increased only in the acute phase but not in the delayed phase.

We demonstrated that neural damage occurred in a biphasic manner after artificial brain injury. We successfully observed by MRI and histological staining that the first damage occurred within 1 week (acute phase), and subsequent damage occurred more than 2 weeks after the brain injury (delayed phase). Since delayed neural damage was not observed in iNOS-KO mice, iNOS expression seems to be responsible for tissue destruction in delayed neural damage. We also found that activated microglia cells were the major cells that expressed iNOS in the delayed phase (Fig. 3C). Most of the activated microglia cells were iNOS-positive and did not produce pro-inflammatory cytokine, IL-1β, in the delayed phase, whereas only some of the activated microglia cells were positive for iNOS with IL-1β expression in the acute phase (Fig. 3C and D). In this study, a brain injury model produced by cerebral ethanol injection was used because the migration of invasive hematopoietic cells such as monocytes and macrophages is hardly induced [21,22]. Then, although monocytes and macrophages as well as microglia cells express Mac-1 (CD11b) antigens [14], accumulated Mac-1-expressing cells originate from endogenous microglia. Since the local production of pro-inflammatory cytokines initiates inflammatory responses, the activation of microglia in the acute phase might be involved in the inflammatory process. This suggests that activated microglia might play distinct roles between acute and delayed phases after brain injury. Microglial activation was observed to occur in a sequential manner, therefore, the first inflammatory activation might trigger further activation of microglia cells resulting in their toxic conversion, leading to an attack of neuronal tissues with NO and other toxic substances such as ROS.

Several lines of evidence suggest that there are some functional differences between activated microglia; some of them exhibit cytotoxic properties and produce several toxic materials to eliminate damaged cells that are beyond the point of recovery, while others exhibit protective characteristics, including the release of neurotrophic factors and the protection of cells from damage [17,18]. The former state of activated microglia is sometimes referred to as the 'further activated' or 'fully activated' form. These two different characteristics of activated microglia play an important role in the pathophysiology of common disorders such as Alzheimer's disease and Parkinson's disease. Recently, it was reported that [^{11}C]PK11195 PET imaging could successfully distinguish between the two different activated states of microglia [8].

Another possibility is the existence of subtypes of microglia. Microglial cells show a rather uniform distribution in terms of cell numbers throughout the brain with only a minor population in some brain regions. The in situ morphologies of these cells, however, may vary markedly from elongated forms observed adjacent to neuronal fibers to spherical cell bodies with sometimes extremely elaborate branching. Furthermore, human fetal microglia cells display heterogeneity in phenotype identified by CD68 [16]. This heterogeneity gave rise to the hypothesis that these cells are differentially conditioned by their microenvironment and, therefore, also display specific patterns of differential gene expression. For example, mRNAs of TNF-alpha, CD4, and Fc gamma receptor II are differentially expressed in microglia isolated from different areas of the brain [15]. It has been reported that the productions of IL-12 [20] and histamine [9] are different in different subtypes of microglia. Furthermore, the subtypes of microglia show distinct acidification profiles by treatment with pepstatin A [12] and selective clearance of oligomeric beta-amyloid peptide [19]. We observed that morphologies and patterns of iNOS expression were different in the acute and delayed phases. Thus, microglial subtypes may display distinct regulation of the progression of neural damage.

We observed that the total amount of NO end products was lower in injured and uninjured brains of iNOS-KO mice than those of normal mice and that in the delayed phase after injury of iNOS-KO mice the amount slightly increased compared with that in uninjured brain, despite the deficiency in iNOS. Because NO is synthesized by two types of NOS (constitutive and inducible), this increase might have resulted from activation of constitutive NOS.

We have clearly indicated that the progression of neural damage that occurs in the brain of individual living animals can be monitored by MRI. The feasibility of this was confirmed by histochemical analysis; the observed changes in brain damage matched between the two methods (Figs. 1 and 2). In the conventional protocol, neural damage is estimated from brain sections obtained from animals sacrificed at different time points by histochemical analysis, which means that the results do not represent the changes in an individual animal. In this study, MRI was used to continuously provide useful information on the severity of neural damage at the injured area in each living mouse. Thus, it is very important that non-invasive imaging techniques for use on living animals, such as MRI, are developed and adopted in many experiments in place of time-course analysis using tissue sections.

Acknowledgements

This study was supported by the Industrial Technology Research Grant Program from the New Energy and Industrial Technology Development Organization (NEDO) of Japan and the Hori Information Science Promotion Foundation.

References

[1] G.C. Brown, Mechanisms of inflammatory neurodegeneration: iNOS and NADPH oxidase, Biochem. Soc. Trans. 35 (2007) 1119–1121.
[2] G.C. Brown, A. Bal-Price, Inflammatory neurodegeneration mediated by nitric oxide, glutamate, and mitochondria, Mol. Neurobiol. 27 (2003) 325–355.
[3] B Bubner, K. Gase, I.T. Baldwin, Two-fold differences are the detection limit for determining transgene copy numbers in plants by real-time PCR, BMC Biotechnol. 4 (2004) 14.
[4] H.M. Gao, B. Liu, W. Zhang, J.S. Hong, Synergistic dopaminergic neurotoxicity of MPTP and inflammogen lipopolysaccharide: relevance to the etiology of Parkinson's disease, FASEB J. 17 (2003) 1957–1959.
[5] J. Garthwaite, Concepts of neural nitric oxide-mediated transmission, Eur. J. Neurosci. 27 (2008) 2783–2802.
[6] C.L. Gibson, T.C. Coughlan, S.P. Murphy, Glial nitric oxide and ischemia, Glia 50 (2005) 417–426.
[7] M.E. Gotz, G. Kunig, P. Riederer, M.B. Youdim, Oxidative stress: free radical production in neural degeneration, Pharmacol. Ther. 63 (1994) 37–122.
[8] F. Ito, H. Toyama, G. Kudo, H. Suzuki, K. Hatano, M. Ichise, K. Katada, K. Ito, M. Sawada, Two activated stages of microglia and PET imaging of peripheral benzodiazepine receptors with [^{11}C]PK11195 in rats, Ann. Nucl. Med. (2010), doi:10.1007/s12149-009-0339-0, in press.
[9] Y. Katoh, M. Niimi, Y. Yamamoto, T. Kawamura, T. Morimoto-Ishizuka, M. Sawada, H. Takemori, A. Yamatodani, Histamine production by cultured microglial cells of the mouse, Neurosci. Lett. 305 (2001) 181–184.
[10] B. Moreno-Lopez, D. Gonzalez-Forero, Nitric oxide and synaptic dynamics in the adult brain: physiopathological aspects, Rev. Neurosci. 17 (2006) 309–357.
[11] K. Nakai, M.B. Kadiiska, J.J. Jiang, K. Stadler, R.P. Mason, Free radical production requires both inducible nitric oxide synthase and xanthine oxidase in LPS-treated skin, Proc. Natl. Acad. Sci. U.S.A. 103 (2006) 4616–4621.
[12] M. Okada, S. Irie, M. Sawada, R. Urae, A. Urae, N. Iwata, N. Ozaki, K. Akazawa, H. Nakanishi, Pepstatin, A induces extracellular acidification distinct from aspartic protease inhibition in microglial cell lines, Glia 43 (2003) 167–174.
[13] K. Ono, K. Fuma, K. Tabata, M. Sawada, Ferritin reporter used for gene expression imaging by magnetic resonance, Biochem. Biophys. Res. Commun. 388 (2009) 589–594.
[14] V.H. Perry, D.A. Hume, S. Gordon, Immunohistochemical localization of macrophages and microglia in the adult and developing mouse brain, Neuroscience 15 (1985) 313–326.
[15] L. Ren, B. Lubrich, K. Biber, P.J. Gebicke-Haerter, Differential expression of inflammatory mediators in rat microglia cultured from different brain regions, Brain Res. Mol. Brain Res. 65 (1999) 198–205.
[16] P. Rezaie, K. Patel, D.K. Male, Microglia in the human fetal spinal cord—patterns of distribution, morphology and phenotype, Brain Res. Dev. Brain Res. 115 (1999) 71–81.
[17] M Sawada, H. Sawada, T. Nagatsu, Effects of aging on neuroprotective and neurotoxic properties of microglia in neurodegenerative diseases, Neurodegener. Dis. 5 (2008) 254–256.
[18] M. Sawada, A. Suzumura, T. Marunouchi, Cytokine network in the central nervous system and its roles in growth and differentiation of glial and neuronal cells, Int. J. Dev. Neurosci. 13 (1995) 253–264.
[19] E. Shimizu, K. Kawahara, M. Kajizono, M. Sawada, H. Nakayama, IL-4-induced selective clearance of oligomeric beta-amyloid peptide(1-42) by rat primary type 2 microglia, J. Immunol. 181 (2008) 6503–6513.
[20] A. Suzumura, M. Sawada, T. Takayanagi, Production of interleukin-12 and expression of its receptors by murine microglia, Brain Res. 787 (1998) 139–142.
[21] A. Takeuchi, K.I. Isobe, O. Miyaishi, M. Sawada, Z.H. Fan, I. Nakashima, K. Kiuchi, Microglial NO induces delayed neuronal death following acute injury in the striatum, Eur. J. Neurosci. 10 (1998) 1613–1620.
[22] H. Toyama, K. Hatano, H. Suzuki, M. Ichise, S. Momosaki, G. Kudo, F. Ito, T. Kato, H. Yamaguchi, K. Katada, M. Sawada, K. Ito, In vivo imaging of microglial activation using a peripheral benzodiazepine receptor ligand: [11C]PK-11195 and animal PET following ethanol injury in rat striatum, Ann. Nucl. Med. 22 (2008) 417–424.
[23] S.P. Zehntner, L. Bourbonniere, M. Hassan-Zahraee, E. Tran, T. Owens, Bone marrow-derived versus parenchymal sources of inducible nitric oxide synthase in experimental autoimmune encephalomyelitis, J. Neuroimmunol. 150 (2004) 70–79.